Image Registration of Lung CT Scans for Monitoring Disease Progression

Gorbunova, Vladlena

Publication date:
2010

Document version
Early version, also known as pre-print

currents, $\lambda_V = 25$ mm, $\gamma_C = 1$, $\gamma_S = 0.01$ and the regularization parameter $\gamma_\phi = 10^{-4}$.

4.4.3 Setup of the Intensity-based Registration

For the intensity-based registration Section 4.3.2, three levels of B-Spline transform $N = 3$ were applied in the multi-resolution strategy. The size of the B-Spline grid at each level was set to $3 \times 3 \times 3$ (approx. $94 \times 73 \times 87$ mm), $6 \times 6 \times 6$ (approx. $47 \times 36 \times 43$ mm), and $12 \times 12 \times 12$ (approx. $23 \times 18 \times 22$ mm), respectively. After each level of the transform, the moving image was deformed with respect to the sum of the deformation fields from the previous levels. We used linear interpolation method to reconstruct intensity values in non-grid point voxels.

Each level of the transformation was optimized separately using a stochastic gradient descent algorithm [51]. The numbers of the voxel samples N_s in the optimisation process were chosen proportional to the number of optimized parameters at each level and at least 10^4. For the Affine transform the $N_s = 10^4$ and for the three sequential levels of the B-Spline transform $N_s = (10^4, 10^4, 5 \cdot 10^4)$ voxel samples respectively. The maximum number of iterations was set to $N_i = 1000$ for every level of the transform.

4.4.4 Setup of the Combined Registration

The proposed iterative registration method from the Section 4.3.4 was iterated for the total number of iterations $N = 10$. The internal parameters of the intensity-based module were fixed as described in the Section 4.4.3, whereas the parameters of the current-based module were set differently from registration method in Section 4.3.1. The current-based module was applied after the intensity-based registration, therefore the major deformations were captured by the intensity-based registration thus the remaining deformations were expected to be smaller than the full deformations. Therefore, we decreased the internal parameters of the subsequent current-based registration module to $\lambda_W = 2.5$ mm for both vessel and surface currents, $\lambda_V = 25$ mm and $\gamma_\phi = 10$ for all the subsequent iterations. The coefficient λ from (4.3) was set to 5×10^3 for all the iterations.

The weight image $w(\mathbf{x})$ was constructed as follows, first the lung surfaces were extracted from the segmented lung regions. Reliable segmentation of vessels and lung surfaces near the hilum area is a difficult task, therefore we erased the lung surfaces and vessel centerlines near the hilum area by first dilating the left and right main bronchus with a disk element of radius 20 voxels in axial plane and then deleting the constructed dilation from the lung surfaces and vessel centerlines. We computed the distance map to the lung surfaces and vessel centerlines and evaluated the Gaussian kernel with the size $\kappa_w = 5.0$ mm on the distance image. Figure 4.3 shows an axial, a coronal and a sagittal slice of a weight image.

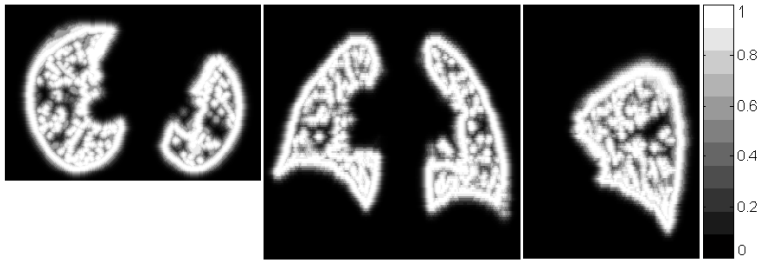

Figure 4.3: An example showing from left to right axial, sagittal and coronal slices of a spatially varying weight image $w(\mathbf{x})$.

4.5 Results

The overall accuracy of a registration method was defined as the average Euclidean distance between the landmarks, target registration error (TRE), in millimeters. For each image pair 300 manually placed landmarks were available in the study [39].

Table 4.2: The target registration error (TRE) in [mm] is reported.

It	TRE [mm]
1	2.39 ± 2.16
2	1.91 ± 1.79
3	1.79 ± 1.56
4	1.79 ± 1.46
5	1.74 ± 1.36
6	1.73 ± 1.29
7	1.72 ± 1.27
8	1.72 ± 1.25
9	1.71 ± 1.24
10	1.71 ± 1.23

The average and the standard deviation of the TRE was obtained from the complete set of 3000 landmarks. Evaluation of the combined image registration approach at each iteration averaged over the complete set of images is reported in the Table 4.2. Figure 4.5a shows the evolution of the mean TRE for each case individually and Figure 4.5b shows boxplots of the TRE for each iteration of the proposed combined registration algorithm.

The TRE of the three registration methods with only the intensity term, described in the Section 4.3.2, the current-based registration, described in the Section 4.3.1, and the proposed iterative combined registration, described in Section 4.3.3 are compared in the Table 4.3. The overall mean and standard deviation before the registration was 8.69 ± 5.99 mm. The TRE after the image registration procedure was reduced to 1.71 ± 1.23 mm, 2.39 ± 2.16 mm and 3.45 ± 3.91 mm for the proposed combined registration, the intensity-based and the current-based registration respectively. The decrease of the average target registration error with the proposed combined registration ranged from -17.8% to 55.4% or -0.21 mm to 2.78 mm compared to the average TRE of the intensity-based registration. The average improvement of the proposed registration method over the intensity-based registration method was 28.5% or 0.68 mm.

Figure 4.4 illustrates how the vessel centerlines were deformed during the

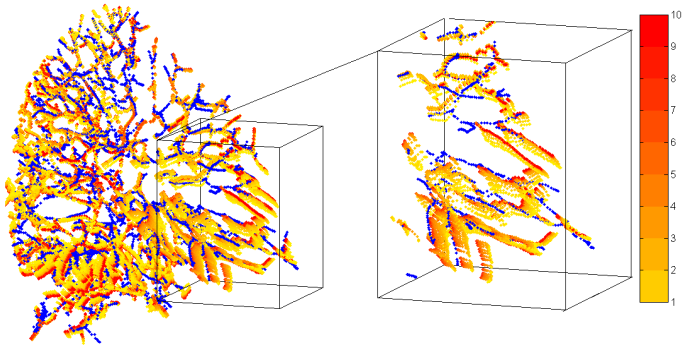

Figure 4.4: Vessel centerlines of the moving image (blue curves) are overlaid with the deformed vessels centerlines of the fixed image (yellow to red curves). Deformed vessel centerlines are displayed in colors ranging from yellow to red with respect to the iteration number of the iterative registartion algorithm.

iterations of the proposed combined registration method. Vessels in the upper part of the lungs were correctly matched already after the first iteration of the algorithm however alignment of the vessels in the lower part was inaccurate. The proposed combined registration gradually improved alignment of the vessels in the lower part of the lungs.

Visual comparison of the intensity-based registration with the proposed combined registration is presented in the Figures 4.6-4.7. Images were first masked using the segmented lung regions and background value was set to 0HU. Then the moving image was deformed with respect to the obtained deformation field, interpolated using linear interpolation and subtracted from the fixed image. Figure 4.6 shows the only example where the proposed registration algorithm resulted in the larger TRE 1.39 ± 0.96 mm than the intensity-based registration algorithm 1.18 ± 0.57 mm. Figure 4.7 shows another extreme case, where the proposed registration algorithm resulted in the largest decrease of the TRE 2.24 ± 2.18 mm compared to the 5.02 ± 3.96 mm.

4.6 Discussion

Recently, Hub et al. [47] showed that an intensity-based registration of lung CT scans is more reliable in areas with clearly defined vessels, while areas without distinctive features were registered generally less accurate. Since an optimization process of sum of square difference similarity function is driven by gradient of the moving image, intensity-based registration method will result in less certain alignment of small, peripheral vessels. Conversely feature-based registration methods rely less on the original intensities and generally include additional information such as connectivity, filter responses, or shape models. In the current-based registration method, described in Section 4.3.1, the segmented vessel tree and lung

Table 4.3: The mean and standard deviation of target registration error at the landmark positions in [mm] before the registration (Original); after the current-based registration (Curr); after the proposed combined registration (Comb It#); and after the intensity-based registration (Intensity).

N	Original	Combined at It#10	Intensity-based	Current-based
1	3.89 ± 2.78	1.39 ± 0.96	1.18 ± 0.57	1.47 ± 0.72
2	4.34 ± 3.90	1.17 ± 0.56	1.26 ± 0.68	2.19 ± 1.98
3	6.94 ± 4.05	1.39 ± 0.75	1.91 ± 1.15	3.30 ± 3.05
4	9.83 ± 4.86	1.70 ± 1.03	2.12 ± 1.52	3.34 ± 2.67
5	7.48 ± 5.51	1.87 ± 1.45	2.23 ± 1.79	3.83 ± 3.54
6	10.89 ± 6.97	1.98 ± 1.07	1.98 ± 1.11	2.85 ± 1.67
7	11.03 ± 7.43	1.85 ± 1.11	2.99 ± 2.09	3.61 ± 4.05
8	14.44 ± 7.16	2.24 ± 2.18	5.02 ± 3.96	5.59 ± 7.01
9	9.24 ± 3.54	1.85 ± 1.06	2.05 ± 1.06	2.89 ± 2.07
10	7.63 ± 6.04	1.72 ± 1.12	2.50 ± 2.11	5.47 ± 5.66
All	8.69 ± 5.99	1.71 ± 1.23	2.39 ± 2.16	3.45 ± 3.91

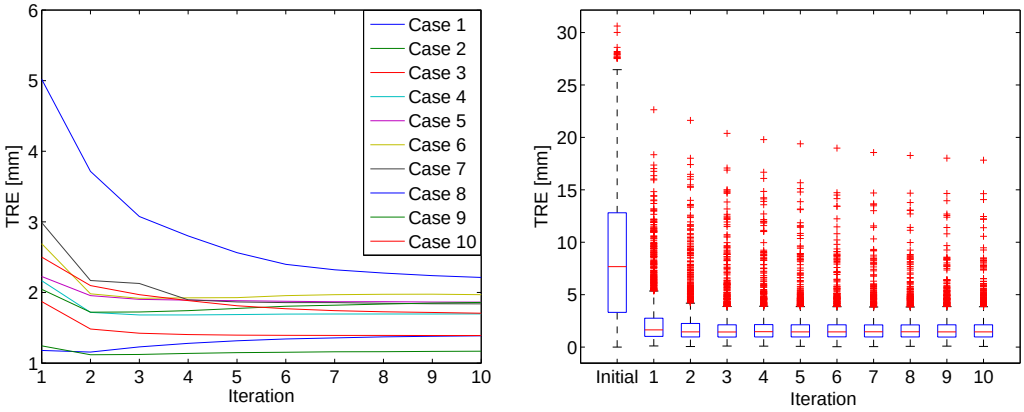

(a) (b)

Figure 4.5: Average target registration error [mm] evolution during the iterations of the combined registration method for every image pair in the study, plot (a). Overall distribution of the TRE [mm] showed in the box-plot (b).

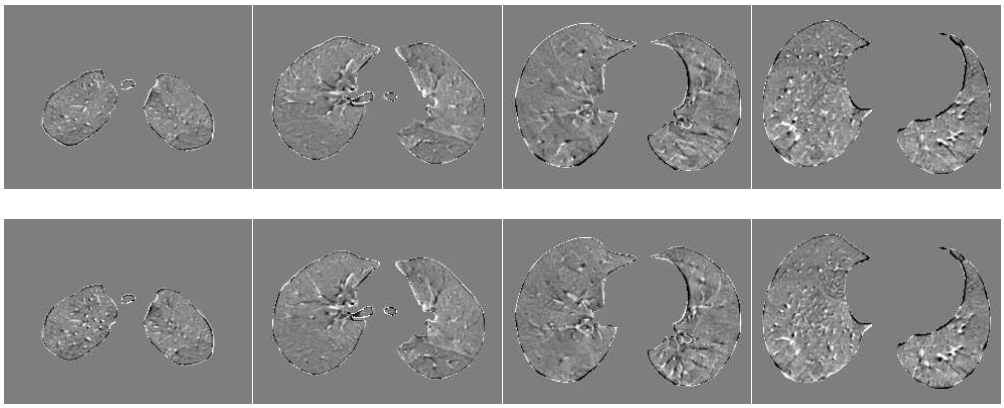

Figure 4.6: The difference images of the intensity-based registration (first row) and the corresponding difference images of the combined registration (second row) for the case #1. The TRE of the intensity based registration was 1.18 ± 0.57 mm and 1.39 ± 0.96 mm for the two registration methods respectively. The difference images are displayed in the intensity range $[-300; 300]$HU.

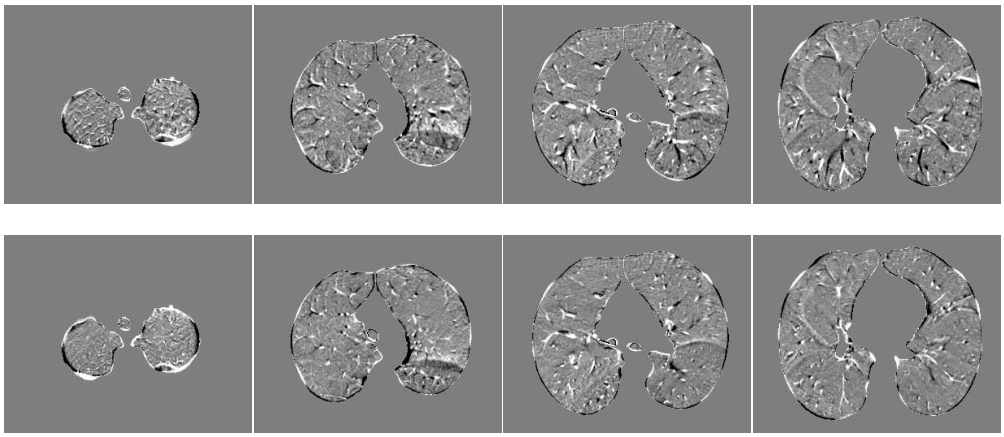

Figure 4.7: The difference images of the intensity-based registration (first row) and the corresponding difference images of the combined registration (second row) for the case #8. The TRE of the intensity based registration was 5.02 ± 3.96 mm and 2.24 ± 2.18 mm for the two registration methods respectively. The difference images are displayed in the intensity range $[-300; 300]$HU.

surfaces are represented with the set of unit vectors regardless of the original image intensities. Thus large and small vessels are assigned the same weight in the feature-based registration and are equally important in the registration.

Assuming that the feature-based registration aligns unclear structures like peripheral vessels better than the intensity-based registration we incorporated the deformations of the segmented features into the intensity-based registration

via a spatially varying weight. The maximum weight of 1 is at the lung borders and the vessel centerlines and decays elsewhere, thus implies the perfect fit of the deformation fields at the location of the segmented structures. However, the actual effect of the constraint propagates within the support of the closest B-spline basis functions. Thus final solution brings minimum both to the sum of squared intensity differences far from an anatomical structure and the differences in the deformation fields close to it.

The proposed combined approach resulted in more accurate registration assessed via the set of manually selected landmarks. The average target registration error was 1.71 ± 1.23 mm for the proposed combined method compared to the intensity-based registration alone 2.39 ± 2.16 mm and the current-based registration of features 3.45 ± 3.91 mm. The registration errors were comparable with the results reported in another study [56], where the registration procedure was applied to only the first three cases and the final accuracy was computed on an extended set of landmarks. The reported average target registration error was 1.59 mm.

In nine out of ten cases, the proposed combined method outperformed the intensity-based registration. The case where the average target registration error increased after the combined registration is displayed in Figure 4.6. Although the increase in TRE was statistically significant, there were no major mis-registrations in the final difference images. While in the another extreme case in Figure 4.7, where the combined registration significantly decrease TRE compared to the intensity-based method, alignment of the vessels was visibly better.

Several reasons may lead to a significantly higher TRE for the current-based registration alone. First, appearance of the vessels in the end inhale and the end exhale phases of the 4D-CT scans varies significantly therefore reliable segmentation with a fully-automatic method is difficult to obtain. Furthermore, centerline extraction is difficult to reproduce with the voxel size accuracy. Figure 4.8 shows an example where the segmented vessel centerlines did not resemble vessels because of the apparent motion artifacts and abnormalities presented in the image. Second, current-based registration alone was performed on twice larger scale than the current-based registration in the combined approach. A more consistent comparison should be performed where a current-based registration is applied in multi-resolution strategy.

The registration task of lung CT scans, where intensity abnormalities presented only in one of the images could be one of the potential applications of the proposed combined registration. Another application could be registration of lung vasculature with attached nodules, where accurate registration of vessels is a key issue in nodule growth analysis.

To conclude, in this chapter we presented a general framework for combin-

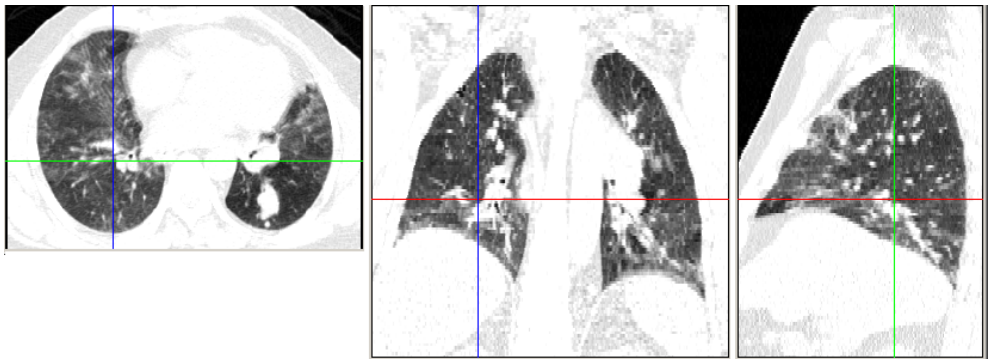

(a)

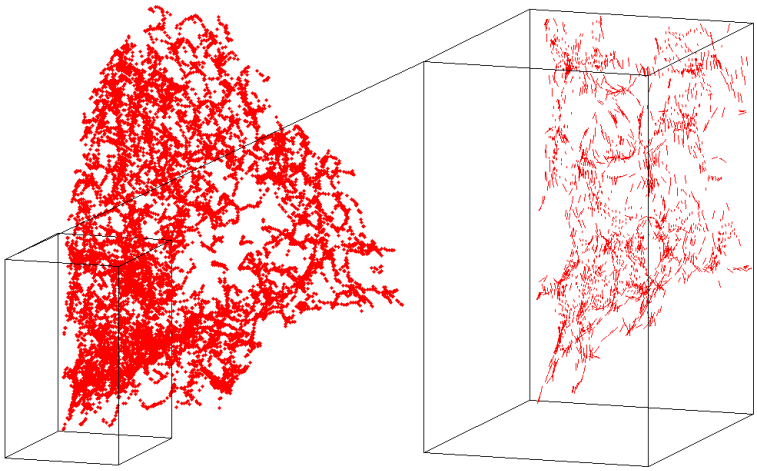

(b)

Figure 4.8: An example of a difficult case (#6), where the vessel centerlines were unreliable. Plot (a) shows an axial, a sagittal and a coronal slices of the original image, plot (b) shows the corresponding vessel centerlines of the right lung and zoom with the constructed currents.

ing feature-based and intensity-based registration methods via incorporating a constraint on deformation field. We combined the previously developed current-based registration of anatomical lung structures with an intensity-based registration method and applied it to ten image pairs of end inhale and end exhale phases extracted from 4D-CT images. The proposed registration method performs better than the feature-based method and the intensity-based method alone. The improvement assessed using a set of manually selected landmarks was on average 28.5% or 0.68 mm compare to the intensity-based method and 50.4% or 1.74 mm compare to the current-based registration methods.

Chapter 5

Evaluation of Methods for Pulmonary Image Registration 2010: Challenge Results

This chapter is based on the publication "Mass Preserving Image Registration: Results of Evaluation of Methods for Pulmonary Image Registration 2010 Challenge", Gorbunova V., Sporring J., Lo P., Dirksen A., de Bruijne M., to appear in proceedings of Grand Challenges in Medical Image Analysis Workshop in conjunction with Medical Image Analysis and Computer Assisted Intervention Conference 2010.

5.1 Introduction

The EMPIRE challenge was organized in conjunction with the Grand Challenges in Medical Image Analysis Workshop at Medical Image Analysis and Computer Assisted Intervention Conference (http://empire10.isi.uu.nl/). The goal of the challenge was two-fold, first to compare existing registration methods from different research groups on exactly the same dataset; and second to investigate common problems of the existing registration methods.

We applied the mass preserving registration algorithm, described in Chapter 2 for the challenge. Since the challenge was conducted during the last month of my PhD study, further improvements of the mass preserving method are not in the scope of the thesis and should be considered as recommendations to those researchers who decided to work with the similar registration method.

5.2 Evaluation

The goal of this section is to describe evaluation methodology which has been used in the EMPIRE challenge. The methodology was developed by challenge organizers and analysis was performed also by challenge organizers. Here I provide brief overview of the evaluation methodology in order to facilitate understanding of the final results. For details please check the web-page http://empire10.isi.uu.nl.

Evaluation procedure consisted of four main components: alignment of lung boundaries; alignment of major fissures; target registration error between manually annotated point pairs; and analysis of singularities in the deformation field.

5.2.1 Lungs Boundary Alignment Scores

Lung fields were segmented using an automatic hybrid method based on the conventional regional growing technique with an additional error detection step, where an advanced multi-atlas segmentation algorithm was applied for final corrections [109]. Once the lung fields were segmented and lung borders were obtained, two regions in the images were defined. The first region Ω^{out} was the outer region outside the lung fields but within 2 to 20 mm distance from the lung borders; the second inner region Ω^{in} was inside the lung fields also within 2 to 20 mm distance from the lung borders. This procedure was applied for both the fixed and the moving images, thus resulting in total of four regions Ω_f^{in}, Ω_f^{out} and Ω_m^{in}, Ω_m^{out}. Given the deformation field $\vec{D}$ from a registration procedure, all voxels within the two regions in the fixed image were deformed with respect to the deformation field. Voxels which were placed in the opposite region in the moving region were considered as the *wrongly matched voxels*. An example of a wrongly matched voxel is a voxel in the inner region $\mathbf{v} = (x, y, z) \in \Omega_f^{in}$, which was positioned in the outer region in the moving image $(\mathbf{v} + \vec{d}(x, y, z)) \in \Omega_m^{out}$ after applying the deformation $\vec{d}(x, y, z)$. Final error score was the percentage of the *wrongly matched voxels* that belongs to one region in the fixed image but positioned into the opposite region in the moving image.

5.2.2 Major Fissures Alignment Scores

Fissures are important anatomical lung structures which separate lungs into lobes. Human right lung contains three lobes including the upper, middle and lower lobes, while left lung contains only two lobes upper and lower lobes. Both lungs have the major (or oblique) fissures, which separate the upper lobe from the lower lobe in the left lung and upper and middle lobe from the lower lobe in the right lung. Lung lobes can slide along the fissures and result in discontinuous deformations at the lung fissures. Furthermore, fissures are very thin structures and it is particularly difficult to match the fissures accurately. Fissures were seg-

mented using an automatic segmentation algorithm [110] and further inspected and corrected manually if needed. The horizontal fissure which separates upper lobe from the middle lobe in the right lung was not included into the analysis. To assess accuracy of a registration algorithm near the major fissures the same analysis was done as for the lung borders. Inner and outer regions were defined in the fixed and the moving lungs, and the final fissure alignment score was defined as the overall percentage of lung voxels inside the outer or inner regions in the fixed image, which were positioned in the wrong region in the moving image.

5.2.3 Point Correspondence Scores

Lungs boundaries alignment and fissures alignment scores only assessed registration accuracy in the limited area of lung fields. In order to investigate registration accuracy inside the lung fields, corresponding points or landmarks were annotated in the two images. Analysis of the target registration errors between the corresponding landmarks remains the most widely used quantitative measure of accuracy of an image registration algorithm. For the EMPIRE challenge, landmarks were identified semi-automatically as in [23]. For each image pair 100 landmarks well distributed inside the lung fields were annotated. The maximum, minimum and average Euclidean distance between the corresponding landmarks were computed for each image pair in left, right or both lungs. Additionally, average distance between the landmarks in anterior-posterior direction (AP), in superior-inferior direction (SP), and in left-righ (LR) directions was computed for both lungs.

5.2.4 Singularity of Deformation Field Scores

Singularity points in the lung fields were defined as points where determinant of the Jacobian of the transform was below or equal to 0. Determinant of the Jacobian characterizes local deformations, if $det(J(\mathbf{x})) > 1$ then expansion of the fixed image space is observed in the point $\mathbf{x}$ which corresponds to the contraction of the moving image space in the transformed point $\mathbf{y} = T(\mathbf{x})$. Vice verse, $det(J(\mathbf{x})) < 1$ is contraction of the fixed image space at the point $\mathbf{x}$ or expansion of the moving image space in the point $\mathbf{y}$. The percentage of points where $det(J(\mathbf{x})) \leq 0$ was defined as the final singularity score of the registration algorithm.

5.3 Results

Registration was applied on a set of 20 image pairs where each pair was obtained from the same subject. Two image pairs were sheep chest CT scans, the remaining 18 were human lung CT scans. Dataset included images acquired from different

Table 5.1: Table presents total scores of the evaluation procedure for each case, and an average over the complete dataset. Absolute difference between the lung volumes, $\Delta TV = V_f - V_m$, and relative lung volume difference $100 \cdot 2 \cdot \frac{V_f - V_m}{V_f + V_m}$ are given in the table for reference. Symbol * marks sheeps lung CT scan image pairs.

	ΔTV		Total scores averaged over both lungs							
ID	[%]	[L]	Fiss.[%]	Rnk	Bound.[%]	Rnk	Sing.[%]	Rnk	Point[mm]	Rnk
1	-61.66	-2.86	0.0487	11	0.2261	24	0	11.5	5.20	22
2	0.32	0.04	0	15	0.0003	26	0	12.5	0.62	24
3	8.20	0.60	0.0040	27	0.0016	24	0	12	0.76	28
4*	-21.61	-0.42	0	16.5	0.0006	8	0	14	1.11	13
5	2.39	0.11	0	16	0	13	0	13.5	0.35	25
6	-2.29	-0.08	0.0043	15	0	16	0	14	0.36	14
7	-43.92	-3.39	0.7549	11	0.2187	22	0	10	5.08	23
8	-21.72	-1.27	0.0812	18	0.0213	21	0	12.5	1.88	24
9	3.70	0.28	0.0002	16	0.0023	26	0	13	0.94	27
10*	-30.12	-0.62	0	15	0.0055	16	0	13	1.56	12
11	-23.49	-1.39	0.2693	21	0.0896	20	0	11.5	2.27	25
12	0.46	0.03	0.0378	31	0	10	0	14.5	1.32	30
13	8.13	0.35	0.1106	21	0.0030	25	0	13	1.26	24
14	-43.93	-3.00	3.0189	12	0.1691	21	0	9.5	5.42	20
15	5.20	0.29	0	7	0.0003	25	0	12.5	0.77	22
16	19.45	0.47	0.4048	26	0.0010	18	0	13.5	1.34	18
17	4.76	0.25	0.0551	19.5	0	6.5	0	14	1.16	23
18	-46.44	-2.91	5.1067	23	0.0954	21	0	10.5	5.14	22
19	-1.10	-0.06	0	12	0	14	0	14.5	0.65	25
20	-45.63	-2.66	9.9041	28	0.1233	24	0.012	26	6.76	22
All	-14.47	-0.81	0.9900	18	0.0479	19	0.0006	13	2.19	22

phases of 4D-CT and 3D scans, images acquired at maximum inspiration and maximum expiration breathholds. Subjects with severe lung disease as well as relatively healthy subjects were included into the study. In-plane spacing varied from 0.4688×0.4688 mm to 0.9766×0.9766 mm, and slice thickness varied from 0.6 mm to 2.5 mm. Lung masks were provided along with the image pairs by challenge organizers.

Table 5.1 presents total evaluation scores averaged over both left and right lung regions, for reference we included lung volume difference between the fixed and the moving images. For every evaluation score in the Table 5.1, the rank of our registration method is given. The rank indicates the final placement of out mass preserving registration method compare to the other 33 participants. Correlation of the relative lung volume difference with the landmark alignment score was -0.87 ($p < 10^{-6}$); with the lung boundary alignment score was -0.85 ($p < 10^{-5}$); with the fissure alignment score was -0.52 ($p = 0.02$); and with the singularity score $= 0.31$ ($p = 0.18$).

Elaborate results for every case in the study are reported in the Appendix 5.4.

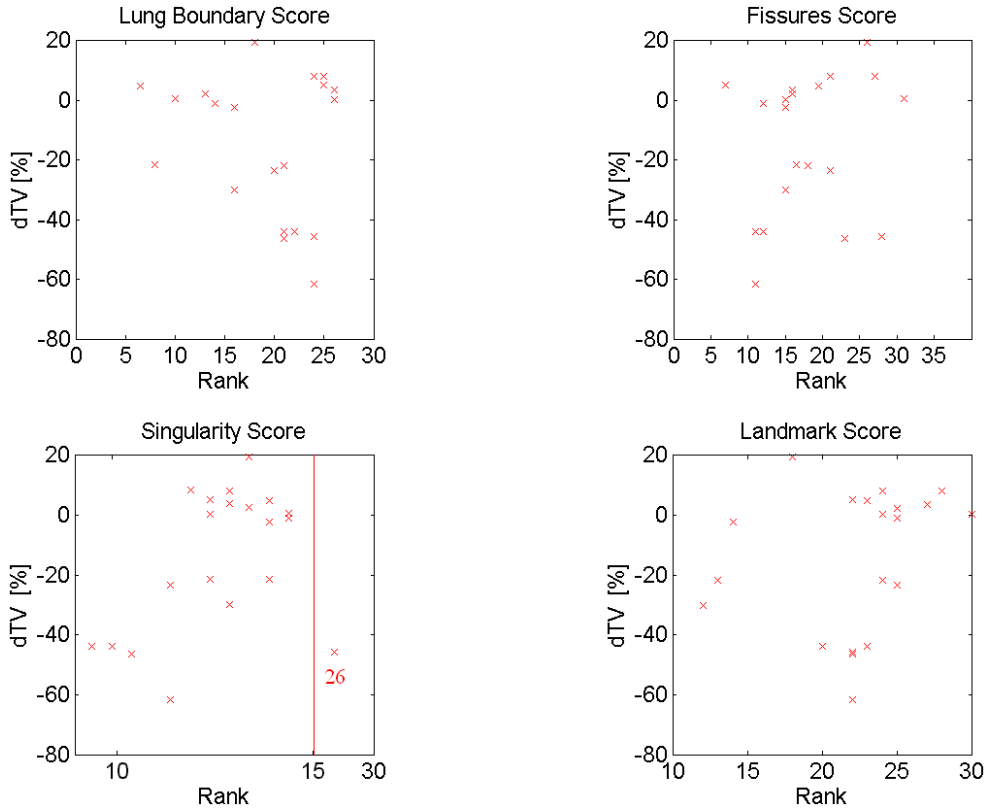

Figure 5.1: Each subplot shows overall rank versus the relative volume difference.

Table 5.2 presents details on the landmark alignment score, the target registration error, computed in only the left or the right lung regions, in the upper or the lower regions of both lungs or over the both right and left lung regions. Additionally, the minimum, maximum and average of target registration error and average distance in anterior-posterior (AR), superior-inferior (SI) and left-right (LR) directions is reported in the Table 5.2. Table 5.3 presents details on the segmentation-based scores computed for only the left or the right lung regions; for only the upper or the lower regions of both lungs or over the both right and left lung regions.

Figure 5.1 displays relationship between the ranking of the mass preserving registration and the relative lung volume difference between the fixed and the moving images.

In order to investigate spatial properties of the mass preserving registration method, we performed Student's t-test between the scores for the right and the left lung regions, between the scores for the top and the bottom regions of both lungs and between the three spatial directions AP, SI and LR. The following scores differ significantly:

- Alignment of the upper part of lung boundaries 0.0033% is significantly

better than the alignment of the lower part of lung boundaries 0.0826%, the corresponding p-value 0.014;

- Landmark alignment in the upper part 1.92 mm is significantly smaller than landmark alignment in the lower part 2.49 mm, $p = 0.030$;

- Landmark alignment in the LR direction 0.75 mm is significantly smaller than both alignment in AP 1.24 mm and SI 1.13 mm directions, with the corresponding p-values 0.0034 and 0.0097 respectively.

5.4 Discussion

Data analysis showed clear asymmetry in the fixed and the moving images. Lung CT scan with smaller lung volume in the image pair were usually set as the fixed image in the registration framework. The relative volume difference between the lungs of the fixed and the moving images was on average $\Delta\text{TV} = 100 \cdot \frac{V_f - V_m}{(V_f + V_m)/2} = -14.47\%$. This potentially leads to a more difficult registration problem than if the image with the bigger lung volume is chosen as the fixed image. In the mass preserving registration, the moving image is being deformed and interpolated after every level of the transform. Shrinkage of the moving image results in the increase of the density of lung parenchyma thus making lung parenchyma less distinguishable from the vessels. In the opposite case, the moving image is expanded and intensity of lung parenchyma decreases potentially leading to a more accurate alignment of vessels.

In 19 out of 20 cases, the proposed method produced invertible deformations. In the remaining case only for negligible percentage of voxels 0.01 % singularities occurred. Since we did not include the regularizer as a part of the cost function, we can conclude that with the multi-level transform strategy and the current setup of the optimization procedure we almost achieved invertibility of the transformation.

Overall mass preserving registration achieved an average landmark alignment score of 2.19 ± 2.05 mm and the median was 1.29 mm. The average ranking for this score 22.15 was larger than average ranking for the remaining scores, ranging from 13.28 to 19.03. One of the reasons for large landmark alignment score could be in a large B-Spline grid, the average size of the B-Spline grid at the final transform level was $2.4 \times 1.8 \times 2.3$ cm^3. Although it could be further improved by applying additional levels of B-Spline transform with smaller grid size, it will also lead to the increase of the complexity of the image registration algorithm. In all the 5 cases, where the average landmark alignment score was above 5 mm, optimization procedure was stopped because of the maximum number of iterations 1000 was reached. This could be improved by increasing the number of maximum iterations.

Figure 5.1 shows weak trend between the rank of the mass preserving registration algorithm and the relative lung volume difference for the fissure alignment and singularity scores. For the scan pairs with large lung volume difference, the mass preserving image registration method was generally ranked higher.

The mass preserving registration method was ranked 20th out of 34 participants. Consider the fact that number of degrees of freedom in the transformation function was relatively small, we conclude that our registration algorithm was able to capture lung deformations with a relatively simple deformation model with acceptable spatial accuracy of 2.19 mm.

Table 5.2: Table presents the complete set of evaluation scores based on the corresponding set of landmarks including average TRE in millimeters in only the left or the right lungs; average distance in anterior-posterior (AR), superior-inferior (SI) and left-right (LR) directions; in the lower or the upper parts of both lungs; minimum, maximum and the average TRE in the complete set of landmarks. Symbol * marks sheep lung CT scans.

	Point Correspondence Scores [mm]									
ID	Left	Right	AP	SI	LR	Upper	Lower	min	max	Average
1	5.86	4.70	3.45	2.51	1.77	4.97	5.42	0.68	19.69	5.20
2	0.64	0.59	0.26	0.28	0.27	0.51	0.73	0.00	1.72	0.62
3	0.85	0.66	0.30	0.26	0.41	0.61	0.91	0.00	3.58	0.76
4*	0.90	1.32	0.59	0.56	0.38	1.41	0.81	0.00	8.98	1.11
5	0.33	0.37	0.14	0.15	0.14	0.25	0.46	0.00	1.63	0.35
6	0.39	0.33	0.15	0.14	0.10	0.32	0.38	0.00	1.62	0.36
7	4.51	5.72	3.06	2.32	2.07	3.81	6.43	0.00	17.04	5.08
8	1.57	2.16	1.13	0.91	0.67	1.55	2.16	0.00	9.13	1.88
9	0.74	1.10	0.42	0.43	0.35	0.71	1.18	0.00	4.26	0.94
10*	0.86	2.28	1.01	0.67	0.52	2.42	0.73	0.00	14.78	1.56
11	3.42	1.47	1.25	1.32	0.68	0.97	3.82	0.00	16.65	2.27
12	1.24	1.39	0.81	0.53	0.52	1.14	1.46	0.00	6.16	1.32
13	1.10	1.48	0.54	0.65	0.54	1.21	1.31	0.00	9.86	1.26
14	3.54	7.16	3.53	2.57	1.55	4.40	6.49	0.00	19.00	5.42
15	0.69	0.84	0.39	0.34	0.29	0.65	0.87	0.00	5.49	0.77
16	1.13	1.47	0.49	0.78	0.45	0.91	1.74	0.00	5.09	1.34
17	0.92	1.43	0.52	0.58	0.39	0.87	1.54	0.00	4.50	1.16
18	3.75	6.43	3.21	2.87	1.46	4.20	6.08	0.00	15.18	5.14
19	0.62	0.67	0.30	0.27	0.25	0.50	0.83	0.00	2.71	0.65
20	8.93	4.98	3.16	4.47	2.20	7.00	6.42	0.64	20.34	6.76
All	2.10	2.33	1.24	1.13	0.75	1.92	2.49	0.07	9.37	2.20

Table 5.3: Table presents the complete set of segmentation-based evaluation scores computed in only the left or the right lung or in both lungs. Additionally, lung boundary alignment score was computed in only the top or the bottom parts of both lungs. Symbol * marks sheeps lung CT scan image pairs.

	Fissure Alignment Scores [%]			Boundary Alignment Score [%]				
ID	Left	Right	Total	Left	Right	Upper	Lower	Total
1	0.17459	0.0179002	0.0485731	0.170507	0.28429	0.00273874	0.386644	0.226142
2	0	0	0	0.00057818	0	0	0.000552154	0.000299014
3	0.0152027	0	0.00396923	0.00184373	0.00134262	0.0011553	0.00201998	0.00160423
4*	0	0	0	0.00151906	0	0.00126241	0	0.000628783
5	0	0	0	0	0	0	0	0
6	0	0.00708509	0.00431069	0	0	0	0	0
7	0.611073	0.920477	0.754927	0.260655	0.172568	0.00333274	0.381276	0.218733
8	0.0934568	0.0728086	0.0812415	0.0248915	0.0175348	0	0.0383258	0.0213195
9	0	0.000338741	0.000218947	0.00418127	0.000239068	0.000399101	0.00385775	0.00225434
10*	0	0	0	0.0126541	0.000396052	0.011021	1.38E-05	0.00549563
11	0.800645	0.00686595	0.269345	0.164437	0.0150489	2.51E-05	0.15856	0.0896095
12	0	0.0573747	0.0378424	0	0	0	0	0
13	0.134571	0.0663076	0.110621	0.00123178	0.00490996	0.000173452	0.00553673	0.00304393
14	5.29557	1.03882	3.01887	0.128602	0.209147	0.0295364	0.29218	0.169147
15	0	0	0	0.000501205	0	0	0.000466908	0.000257115
16	0.148368	0.485892	0.404845	0.00131663	0.000769482	0	0.00184002	0.00104999
17	0.142005	0	0.0551116	0	0	0	0	0
18	12.183	0.493686	5.10668	0.112339	0.0779893	0.00570641	0.166464	0.0954141
19	0	0	0	0	0	0	0	0
20	14.2453	7.22431	9.90405	0.0939973	0.153227	0.0108393	0.214154	0.123334
All	1.692189075	0.519593294	0.990030273	0.048962738	0.046873109	0.003309496	0.082594555	0.047916607

Chapter 6

Mass Preserving Image Registration For Monitoring Emphysema Progression

This chapter is based on the publication "Weight Preserving Image Registration For Monitoring Emphysema Progression", Gorbunova V., Lo P., Ashraf H., Dirksen A., Nielsen M., de Bruijne M., in proceedings of Medical Image Computing and Computer Assisted Intervention Conference in 2008.

6.1 Introduction

Chronic Obstructive Pulmonary Disease (COPD) is the fourth leading cause of death in the world [5]. COPD encompasses both small airway disease and emphysema which is characterized by the destruction of lung parenchyma. The current gold standard for diagnosing COPD is based on lung function tests (LFT) such as the forced expiratory volume in one second (FEV1) and forced vital capacity (FVC). These methods are well suited for diagnosing COPD but lack the sensitivity and reproducibility to detect mild emphysema or small changes in disease status.

CT analysis allows the quantification of emphysema with a higher accuracy, even in early stages. Emphysematous regions appear as areas with low-attenuation in CT scans of the lungs, suggesting that CT image intensities can be used to quantify the severity of emphysema. Averaged lung density, n-th percentile density, and relative area with attenuation below, e.g., -910HU (em-

physema index, RA-910HU) have all been successfully applied as emphysema measures. However, current CT emphysema measures have two major drawbacks: measurements are averaged over the complete lung region, which makes it difficult to detect small and localized differences, and they are strongly influenced by variations in the inspiration level [17]. For accurate monitoring of disease development and progression one should be able to analyze regional changes. We propose to use image registration for this purpose. Non-rigid image registration of lung CT scans has previously been used as an aid in determining growth of lung nodules [74], but to our knowledge has not been applied to longitudinal studies of emphysema.

There exist two fundamentally different approaches to analyzing regional changes in longitudinal studies or image sequences using registration. One approach considers an almost perfect registration and subsequently analyzes the deformation field. This approach has for example been applied to lung SPECT and CT scans to analyze breathing motion [53]. The second approach aims at compensating for gross deformation caused by other factors not related to the disease process, and subsequently analyzes the differences in local appearance or intensity between the target and the registered image as a measure of disease progression. The second approach is taken in this chapter: registration is used to correct for expected normal lung deformation and differences in inspiration level between scans, whereas the finer scale disease process of growing and merging emphysema bullae is revealed in the difference images.

In repeated breath-hold scans of the same subject, the difference in total lung volume between scans is often more than a half liter, even if the subjects are instructed to hold their breath at maximum inspiration. This has a large effect on the density of lung tissue in the CT scan and on common density derived measures of emphysema [17]. To correct for differences in inspiration level we used an assumption of total lung mass preservation throughout the respiratory cycle which was discussed previously in [82]. We propose to constrain the image registration to preserve local and global mass of lungs during deformation and adjust voxel intensity values with respect to local volume changes. A composition of affine and multi-level free-form registration was applied to align the baseline scan with the follow up and the obtained difference maps were analyzed for local tissue loss. The main advantages of the proposed method are: (a) it is robust to significant difference in total lung volume between baseline and follow-up scans; (b) it is capable of estimating regional destruction of lung tissue.

6.2 Method

6.2.1 Mass Preserving Image Registration

First baseline image was registered to the system of the coordinates of the follow up image using the mass preserving image registration presented in Chapter 2. Because experiments in this Chapter were conducted in the beginning of my PhD study, the set-up of the registration framework here differs from the Chapter 2. The essential differences are: regions outside of the lung fields were included in the fixed and the moving image regions; a limited memory algorithm for bound constrain optimization [111] was used to minimize the dissimilarity function; and complete set of image voxels in the image was used in the optimization procedure.

Once the correspondence between the two images was obtained, baseline image was deformed and intensities of the baseline image were adjusted with respect to the local volume change measured from the determinant of Jacobian of the transformation.

6.2.2 Measure of disease progression

We first subtracted the registered baseline image from the follow up, thus forming an intensity difference image, where negative areas indicate local loss of lung tissue and thus progression of emphysema. To reduce the effect of noise and interpolation artifacts around vessel boundaries, the resulting difference maps were filtered with a median filter of size $3 \times 3 \times 3$ and masked with the dilated vessel masks and segmented lung regions from both images.

We assumed only voxels $\mathbf{x} = (x, y, z)$ with intensity difference within the interval $(-500; -50)$ are disease-related. The reason for this is to remove artifacts due to interpolation and inaccurate registration and reduce the influence of noise. We compute an average density loss measure μ over overlapping lungs volume V, by summing the disease-related intensity differences, given as:

$$\mu = \frac{1}{V} \sum_{\Omega_D} I_f(\mathbf{x}) - I_b(T(\mathbf{x})), \tag{6.1}$$

where the symbol $\Omega_D = \{\mathbf{x} | I_f(\mathbf{x}) - I_b(T(\mathbf{x})) \in (-500; -50)\}$ denotes the set of voxels with intensity difference within the $(-500; -50)$ HU range.

6.3 Experiments and results

We evaluated the method on a set of 29 low dose CT image pairs collected from the Danish Lung Cancer Screening Trial. The images are selected such that they have a considerable difference in total lung volume (0.6 ± 0.5L) between baseline and follow up scans. The in-plane resolution was 0.78×0.78 mm and the slice thickness was 1 mm. Image pairs have a time interval between baseline and

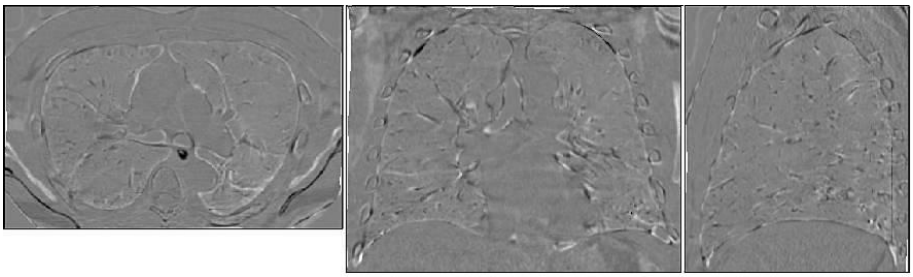

Figure 6.1: A difference image illustrating an example of mass-preserving image registration, showing the deformed baseline image subtracted from the follow up image. From left to right the mid-axial, coronal and sagittal slice is shown.

follow up of approximately one year. Of these, at baseline 11 subjects had no COPD according to the GOLD guidelines [5], 5 were classified as having mild COPD, and 3 as moderate (FEV1/FVC $= 66 \pm 10$). At follow up, 5 subjects are healthy, 11 have mild COPD and 3 have moderate COPD. 10 Image pairs were collected with a 3 month interval, of these 9 subjects had no COPD and 1 had mild COPD (FEV1/FVC $= 74 \pm 4$).

To save computation time, the original CT lung scans were cropped according to the segmented lungs before image registration. A gradient descent algorithm was used for optimizing the parameters of the affine transform. The multi-level B-Spline transform was optimized using the L-BFGS method [36]. The first level was performed on a grid resolution of $3 \times 3 \times 3$ grid points on the image domain, the second level on a resolution of $6 \times 6 \times 6$ grid points and the finest level on a $12 \times 12 \times 12$ or $2.5 \times 2.5 \times 2.5$ cm^3 grid. The first two levels of the B-Spline transform were applied to smoothed and sub-sampled versions of the images whereas the finest level was applied to the original images. The image registration framework was implemented with ITK [69].

Figure 6.1 shows the result of described image registration technique for an arbitrary subject. Differences in subject positioning within the CT scanner and part of the changes in lung volume were corrected via affine registration. The first level of the B-Spline transformation aligned global lung structures such as the lobes and diaphragm. The second level performed on the same resolution as pulmonary segments and adjusted internal lung deformations. Finally, the finest level corrects for deformations in the subsegmental level. Figure 6.1 shows clearly that the majority of internal lung structures is aligned with about 2-3 voxels accuracy; only a few misalignments near the lung and bronchial tree borders remain.

To verify the preservation of mass during the registration procedure, we compute the lung mass for standard and mass-preserving registered images and compare it with corresponding original image characteristics. The mean squared difference between the lung mass of the original baseline image and the regis-

tered image for standard image registration is $1.18 \cdot 10^{-2}$kg, two times more than for the proposed mass-preserving registration technique ($5.09 \cdot 10^{-3}$kg).

Examples of obtained local disease progression maps for four subjects with various values of differences in total lung volume and LFT are shown in Figure 6.2. The areas outside the lung and the vessel masks were excluded from the difference maps. Representative axial slices were chosen close to the carina point.

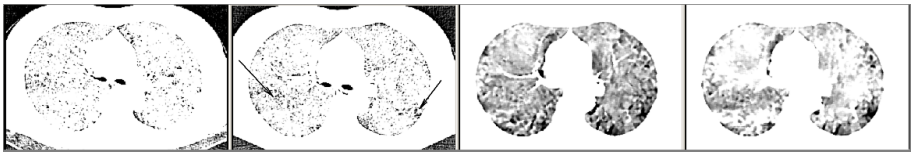

(a) Patient with $\Delta TLV = 0.64L$, mean FEV1/FVC = 69 and decrease in FEV1/FVC = −9.3

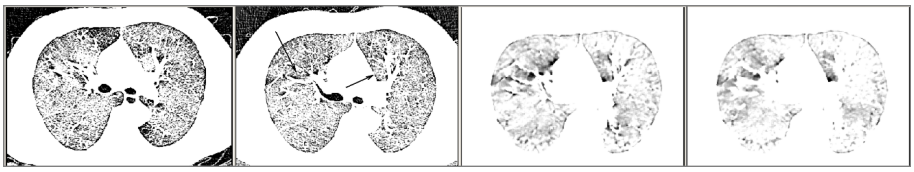

(b) Patient with $\Delta TLV = 0.48L$, mean FEV1/FVC = 68 and decrease in FEV1/FVC = −7.5

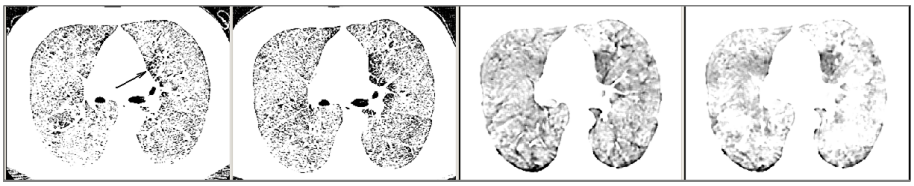

(c) Patient with $\Delta TLV = 1.06L$, mean FEV1/FVC = 65 and decrease in FEV1/FVC = −11.2

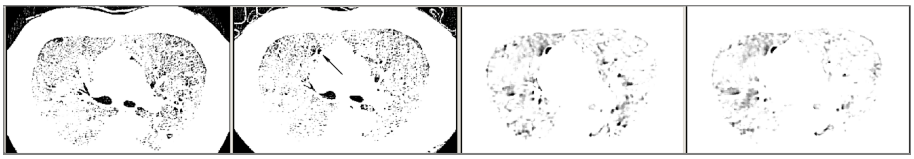

(d) Patient with $\Delta TLV = 0.39L$, mean FEV1/FVC = 69 and decrease in FEV1/FVC = −0.3

Figure 6.2: Left most column shows an axial slice of a baseline scan; second column shows the most corresponding slice on the follow up scan with notable regions of emphysema progression indicated by arrows; third column shows the corresponding slice in difference image for the standard image registration technique; most right column shows difference image for mass-preserving image registration. The original scans were both thresholded at -910HU to reveal emphysematous areas; the difference images were median filtered and viewed at intensity window: 0 to -200.

The resulting measure of disease progression is correlated to changes in RA-

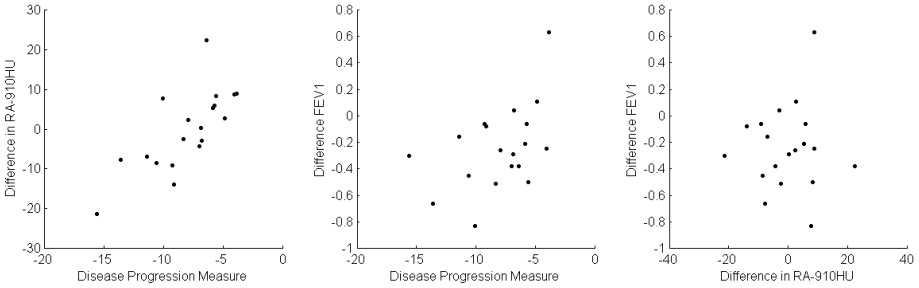

Figure 6.3: Relationship between annual difference in FEV1, difference in RA-910HU, and averaged mass loss in HU computed for the mass-preserving image registration for a group with 1 year time interval.

910HU and difference in FEV1 between baseline and follow up visits. Scattered plots are shown in Figure 6.3 We expect a positive correlation between our measure of disease progression and annual difference in FEV1 but not perfect, since this measure is known to vary substantially [14]. The correlation coefficient between annual difference in FEV1 and the registration based measure for standard registration $\rho_{\text{diffFEV1},\mu} = 0.1$ ($p = 0.69$) and for mass-preserving registration $\rho_{\text{diffFEV1},\mu} = 0.47$ ($p = 0.04$). The correlation coefficient between RA-910HU and registration based measurement for standard case $\rho_{\text{RA-910},\mu} = 0.82$ ($p < 0.01$) and for mass-preserving registration $\rho_{\text{RA-910},\mu} = 0.73$ ($p < 0.01$). The correlation coefficient between RA-910HU and annual difference in FEV1 $\rho_{\text{diffFEV1,RA-910}} = 0.04$ ($p = 0.87$).

To estimate influence of the inspiration level for the standard and mass-preserving image registration techniques we computed the correlation coefficients between difference in total lung volume and proposed disease progression measure for subjects scanned with 3 month interval. The correlation coefficient between the difference in total lung volume and the registration based measure for standard registration $\rho_{\text{diffTV},\mu} = 0.92$ ($p < 0.01$) and for mass-preserving registration $\rho_{\text{diffTV},\mu} = 0.51$ ($p = 0.14$).

6.4 Discussion and Conclusions

The proposed image registration method performed well for cases with considerable total difference in lung volume between baseline and follow up scans, both mass-preserving and standard registration generally align internal lung structures within 2mm.

The proposed mass-preserving image registration maintained the total mass of the lungs better than a standard registration approach. Remaining deviation between the original and registered image mass occurred due to natural limitations of the image registration technique such as the smoothing effect caused by linear interpolation and B-spline transformation.

The first three subjects in Figure 6.2 had a substantial increase in total lung volume from baseline to follow up, causing RA-910HU as well as standard registration to overestimate the changes in emphysema. The mass-preserving difference maps appear less dark in areas where there is no apparent disease progression in the original images. The darker areas in the mass-preserving difference maps correspond to localized areas of local emphysema progression clearly visible in the original images, while the difference maps based on standard image registration suggest a more diffuse tissue loss in the entire lung region. In the fourth case, where the difference in total lung volume was relatively small, both methods performed similar.

Comparison of the average local tissue loss with RA-910HU revealed a good, but not perfect correlation which indicates that the two measures may carry different information. Although we found low correlations with annual difference in FEV1 in this small sample, the measure based on mass preserving registration does seem to agree better with annual difference in FEV1 than do RA-910 and local progression measured using standard registration. This suggests that the proposed method may be more sensitive to subtle changes in disease status. It should be noted that the annual loss of tissue in most subjects with emphysema is very low, especially among normal smokers and mild COPD subjects, which constituted the majority of our test population. In future work we will investigate the proposed measures in a larger sample and with longer follow-up times.

To conclude, we propose an image registration based method for quantification of COPD disease progression which can estimate local destruction of lungs tissue and is less effected by differences in inspiration level than currently available methods.

Chapter 7

Early Detection of Emphysema Progression

None of us is as smart as all of us.

— JAPANESE PROVERB.

This chapter is based on the publication "Early Detection of Emphysema Progression", Gorbunova V., Jasobs S., Lo P., Dirksen A., Nielsen M., Bab-Hadiashar A., de Bruijne M., to appear in proceedings of Medical Image Computing and Computer Assisted Intervention Conference in 2010.

7.1 Introduction

Emphysema is one of the most common chronic obstructive pulmonary diseases [5]. It is characterized by irreversible destruction of the lung parenchyma and usually caused by smoking [112].

In clinical practice, the severity of emphysema is commonly assessed using different lung function tests. Along with the lung function tests chest CT scans has been used for diagnosis of emphysema and detection of emphysema progression. The standard CT density scores, such as relative area (RA) below certain threshold, e.g. -950 HU or -910 HU, and the n-th percentile density (nPD) of the lungs, were applied to estimate the emphysema progression [17, 16]. CT densitometry

scores have shown to be more sensitive measures of emphysema progression than lung function tests [16].

One of the major drawbacks of the standard CT density scores is their dependency on the inspiratory level [31, 29]. Another important drawback is the lack of sensitivity, since the emphysema progression could only be measured once the intensity of lung tissue decreases below the standard threshold. Texture analysis may resolve this problems. This issue was investigated in a recent study, where a texture-based classification approach was proposed as alternative to the standard emphysema scores [113]. The results showed that the texture-based approach outperforms the RA scores in differentiating diseased from healthy subjects.

Several studies proposed how to estimate disease progression from longitudinal CT scans [31, 29]. Authors proposed a method where CT scans are first registered to a common framework and then emphysema progression is estimated based on the average intensity decrease between the two successive scans.

In this chapter, we propose a more general way of assessing emphysema progression between a pair of images. Firstly, images are registered to a common system of coordinates. Secondly, local image histograms at a given location are obtained and dissimilarity measures between the histograms are computed. Thirdly, a measure of progression at the given location is derived from the dissimilarity measures. Finally, an overall disease progression score between the two images is computed. In this chapter, the proposed method is applied to detect emphysema progression in a longitudinal study of patients with Alpha-1 antitrypsin deficiency [16].

7.2 Method

In this section we describe in details the workflow of the algorithm. The first subsection 7.2.1 briefly recalls the image registration method that is applied to establish the spatial correspondence between images. The following subsection 7.2.2 presents how local dissimilarities are constructed. The last subsection 7.2.4 describes how the local disease progression score on subject level is derived from the set of local dissimilarity measures.

7.2.1 Registration

The image registration framework presented in Chapter 2 is used to register the follow up images $I_{2..5}$ to a system of coordinates of the baseline image I_1. The framework starts with a preprocessing step, where the lung fields are extracted from the CT scans and the background value is set to 0 HU. First, an affine transform is applied to correct for global deformations. Then a series of multi-resolution B-Spline transforms with decreasing grid resolution is applied to

the affinely registered images. Each transform is optimized using the stochastic gradient descent method.

Finally, the moving image is deformed based on the obtained deformation field. To minimize the intensity differences in the fixed and moving images caused by the difference in inspiratory level, the intensities of the deformed image are adjusted with respect to the Jacobian determinant of the deformation field as proposed in Chapter 2.

7.2.2 Local Image Features

The registration algorithm results in dense spatial correspondence, but small misregistrations in the order of 1 mm remain. To minimize the impact of the misregistration, we propose to compare points in the different images using a simplified version of locally orderless images (LOI) [114], where the inner, outer and tonal scales where fixed. A local histogram is constructed using a weighted window function centered around a point $\mathbf{x}_0$. Given an image $I(\mathbf{x}_0, \sigma)$ that is observed under the fixed inner scale σ, the LOI at a point $\mathbf{x}_0$ is defined as follows:

$$h_I(i; \mathbf{x}_0, \alpha) = \frac{1}{(\sqrt{2\pi}\alpha)^3} \int_0^{\mathbf{x}} A(\mathbf{x}, \mathbf{x}_0, \alpha) e^{-(I(x,\sigma)-i)^2} d\mathbf{x}, \tag{7.1}$$

where α is the outer scale, which corresponds to the size of the window function $A(\mathbf{x}, \mathbf{x}_0, \alpha) = e^{\frac{(\mathbf{x}-\mathbf{x}_0)\cdot(\mathbf{x}-\mathbf{x}_0)}{2\alpha^2}}$ and i is an intensity value.

In order to capture different features, in addition to the original image I, LOIs are also computed from the blurred image and the gradient magnitude. The feature images are all observed under the same scale, which is achieved by blurring the images using a Gaussian kernel with a standard deviation of σ.

7.2.3 Dissimilarity Measures

Given the two histograms $h_1(i; \mathbf{x})$ and $h_t(i; \mathbf{x})$ obtained in the same anatomical point $\mathbf{x}$ from the two images I_1 and I_t respectively, we compute a set of dissimilarity measures $D(I_1, I_t)(\mathbf{x}) = \{d_i(h_1(i; \mathbf{x}), h_t(i; \mathbf{x}))\}$ between the histograms. Later in text we denote the histograms using shorter notations h_1 and h_t.

In this paper, we use two classes of dissimilarity measures. First class consists of L1-norm and Kullback-Leibler divergence between the two histograms $d_1 = ||h_1 - h_t||_{L_1}$, $d_2 = ||h_1 - h_t||_{L_2}$, $d_3 = D_{KL}(h_1, h_t)$. In the second class, the dissimilarity between the local histograms is computed as difference between the individual measures of each of the histograms $d_i = m_i(h_1) - m_i(h_t)$ [115]: the first four moments, the mode, the energy; and the maximum of difference between the cumulative distribution functions of the histograms $d_n = \max(\mathrm{cdf}(h_1) - \mathrm{cdf}(h_t))$.

7.2.4 Disease Progression Measure

Since LOIs have a certain region of influence, it is not required to compare each and every point in the images. Therefore, a sparse representation of the image is used for comparison instead, where comparison is only performed on a fixed number of regions, N_s, sampled randomly within the lung regions.

For every sample $\mathbf{x}_i$ we compute the set of dissimilarity measures $D_I = D(I_1, I_t)$ between the images I_1 and I_t, and the filtered versions of the images $D_G = D(I_{1,\sigma}, I_{t,\sigma})$, $D_{GM} = D(|\nabla I_{1,\sigma}|, |\nabla I_{t,\sigma}|)$. The subscripts I, G, GM denote the original image and response to the Gaussian and Gaussian magnitude filters respectively. Therefore dissimilarity between the two images at the location $\mathbf{x}_i$ is defined by the dissimilarity vector $\vec{D}_{1,t} = \{D_I, D_G, D_{GM}\}_{1,t}$.

The dissimilarity measures from the first class assess the distance between the corresponding local histograms. The dissimilarity measures from the second class assess the change in the histogram characteristics. If two histograms differ, dissimilarity measures from the first class are strictly positive while the dissimilarity measures from the second class result in both positive and negative values. We are interested in local changes regardless of the sign therefore only the magnitude of the dissimilarity measures is considered. Finally, the measure of local changes $p_{1,t}(\mathbf{x}_i)$ at the sample $\mathbf{x}_i$ between the images I_1 to I_t is computed as the L1-norm of the dissimilarity vector, as follow, $p_{1,t}(\mathbf{x}_i) = ||\vec{D}_{1,t}||_{L_1}$.

7.3 Experiments

7.3.1 Data

We conducted experiments on subjects with Alpha 1-antitrypsin deficiency monitored during a period of 30 months. A total of 27 subjects were included into the experiments. For each subject low-dose CT images were acquired at five time points: at baseline, after 3, after 12, after 21, and after 24 or 30 months. Out of 27 subjects 11 were scanned after 24 months. The scans were acquired using a tube voltage of 140 kVp, exposure 40 mAs, in-plane resolution 0.78 mm and slice thickness 2 mm without overlap.

Lung function tests were acquired along with the CT scans, of which we used the forced expiratory volume in 1 second (FEV_1). At baseline all the patients performed lung function tests and average FEV_1 for all the subjects was 1.54 ± 0.68 L, and TLC was 8.02 ± 1.57 L, the ratio FEV_1/TLC was 20.27 ± 10.38 %. For the last visit there are 2 missing lung function tests, and the average over the remaining 25 subjects is FEV_1 1.29 ± 0.71L, TLC 7.45 ± 2.51 and ratio FEV_1/TLC 17.93 ± 9.04 %.

7.3.2 Measuring Local Emphysema Progression

The four follow up CT scans I_2, I_3, I_4, I_5 were first registered to the baseline image I_1. The segmented lung fields from the baseline image I_1 were eroded with a cubic structuring element of size of $3 \times 3 \times 3$ voxels and $N_s = 2000$ positions were randomly sampled from the eroded lung fields. In our experiments we chose the Gaussian scale of the filters $\sigma = 1$ voxel. The radius of the aperture function A was set to $\alpha = 20$ voxels, and the weights were truncated at 3α radius. For the intensity-based histograms the bin width was set to 1 HU resulting in 1000 bins in total in the intensity range from -1000 to 0 HU. For the histograms of the filtered images, the number of bins was set to 1000 and the bin edges were placed uniformly covering the full range of filter responses.

Within a 3 month period changes are expected to be relatively small, therefore the dissimilarities observed in this period reflects mostly image dissimilarity caused by misregistration and interpolation. From these pairs of images we obtained the mean and the standard deviation of the dissimilarity vector $\vec{D}_{1,2}$. Further we normalized all the dissimilarity vectors $\vec{D}_{1,t=2,3,4,5}$ with respect to the obtained mean and standard deviation and then computed the corresponding progression measures $p_{1,t=2,3,4,5}$.

7.4 Results

Table 7.1 reports the summary of the conventional emphysema progression measurements, the decline in FEV_1 (ΔFEV_1 in L) and increase of relative area below the 950HU(ΔRA950 in [%]). The conventional measures were compared with the proposed feature-based disease progression measures. Disease progression measure (PM) on a subject level was computed as the average of dissimilarity measures for all spatial locations. We tested the complete set of dissimilarities (PM (all)); only Kullback-Leibler divergence between the local histograms of the smoothed images as the local dissimilarity measures (PM (KL)); and only local increase in RA950HU (PM (locΔRA950)). Table 7.1 presents the average disease progression measures for all consecutive follow up visits. A time trend analysis was performed for the disease progression measurements using a linear mixed model with the time between the baseline and a follow up visit as the fixed effect. For the FEV1 we did not conducted time trend analysis because 9 out of 27 subjects had missing FEV1 measurement at least at one of the visits. The t-values are reported in the Table 7.1. Additionally, correlation coefficients between the progression measured at the last visit assessed by either the proposed methods or by the conventional emphysema score or the lung function are presented in the Table 7.2.

Figure 7.1 shows samples locations, indicated with circles, overlaying on the 2D-slices extracted from the baseline and the registered follow up images. Radius

Table 7.1: Summary of the disease progression measures. Left part presents the average of the progression measures over all subjects for the follow up visits and the t-value of the time-trend analysis.

	Average Progression				Time-trend
# mnths	3	12	21	30(24)	t-value
ΔFEV$_1$	-0.03	0.01	-0.01	-0.13	NA
ΔRA950	-1.27	0.08	1.33	1.91	6.37
PM (all)	0.75	0.76	0.89	0.93	3.09
PM (KL)	0.25	0.27	0.30	0.31	7.80
PM (locΔRA950)	0.0	0.46	0.77	1.03	8.80

Table 7.2: The correlation coefficients between the progression measures obtained from the last visit with the corresponding p-values in brackets.

Average Progression	Correlation coefficients	
at 30(24) months	ΔRA950	ΔFEV$_1$
ΔFEV$_1$		
ΔRA950		-0.18(0.48)
PM (all)	0.51(0.007)	0.11(0.59)
PM (KL)	0.45(0.02)	-0.18(0.39)
PM (locΔRA950)	0.87(< 0.001)	0.11(0.59)

of a circle in the follow up images is proportional to the dissimilarity measure computed from the complete set of dissimilarities. Each row displays different subject.

In order to investigate local consistency of the local disease progression measures, we tested the simple hypothesis that samples with dissimilarity measure above a threshold T at the previous follow up visit should not decrease the dissimilarity measure in the consecutive visits. The threshold on the dissimilarity measure was selected based on the 25th- and 75th- percentiles, p_{25} and p_{75}, of the dissimilarity measures after the 3 months follow up visit, $T = p_{75} + 1.5(p_{75} - p_{25})$, which corresponds to ~ 2.7 standard deviations. The total number of samples with dissimilarity above the threshold T and the relative percentage of those samples that increase or preserve the same dissimilarity measure in all the successive visits is reported in the Table 7.3.

Examples of the samples with disease progression measure above the threshold T are presented in the Figure 7.2. Plot in Figure 7.2a displays a subject where most of the samples with the large dissimilarity measure after 3 months were confirmed with all the consecutive follow up scans. Plot in Figure 7.2b displays a subject where the samples did not show consistent dissimilarity measure over time.

Figure 7.1: Rows show mean intensity projection over a stack of 9 sequential slices, selected from different volumetric images. The left most column shows slices extracted from the baseline image, the remaining columns show corresponding slices extracted from the registered 3, 12, 21 and 30(24) months follow up visits, respectively from left to right. All the slices are displayed in the intensity range [-1000,-900]HU. Locations of the random samples (blue and red markers) in the corresponding stack were projected to the image slice. In the follow up images the marker size is proportional to the local dissimilarity measure obtained from the complete set of dissimilarities.

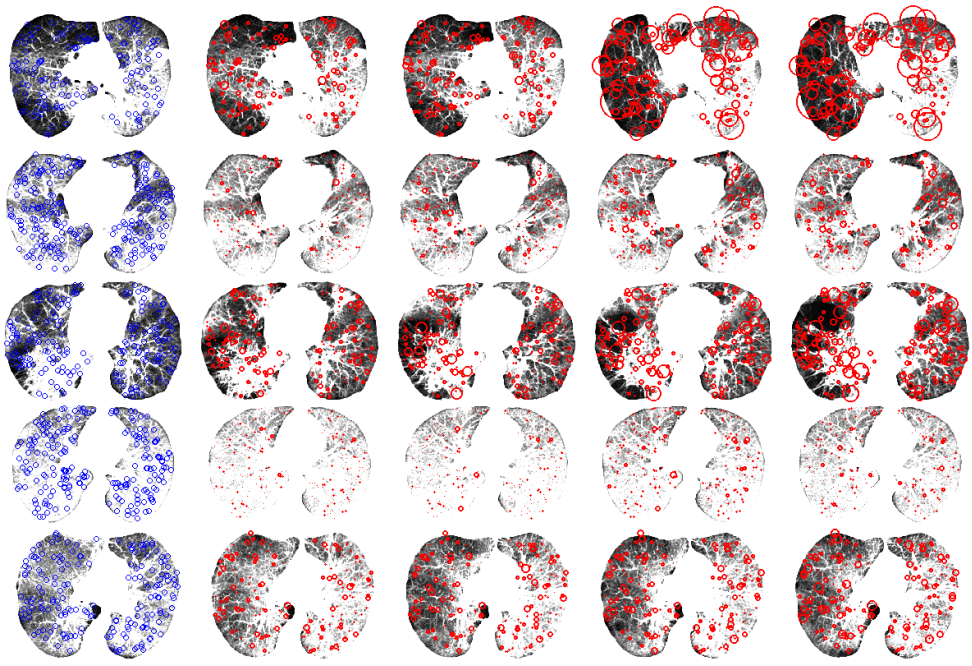

7.5 Discussion

In this chapter we presented a framework for detection of local emphysema progression. The overall disease progression measure showed significant correlation ($p < 0.01$) with increase in the standard CT score, the relative area below -950HU, between the baseline and the last follow up visit. The correlation with the decline in FEV_1 was not significant for neither the proposed measures nor for the standard CT score. In our dataset the average FEV_1 at baseline was very low, indicating the severity of emphysema already at the baseline visit. This can explain the lack of sensitivity to disease progression of the FEV_1 measurement.

We analyzed time trend based on the conventional emphysema measurements and the proposed dissimilarity-based measurements. The time trend was approximately equally significant for the conventional RA950 disease progression measure, local increase in RA950 and the measure derived from the Kullback-

Table 7.3: Comparison of the local dissimilarity measures. Table presents the overall percentage of samples with dissimilarity measure above the threshold T; in brackets the relative percentage of sampled which increased or preserved the dissimilarity measure above the threshold in all the successive follow up scans.

	Overall percentage [%] (confirmed [%])			
# mnths	3	12	21	30(24)
PM (all)	5.24(41.61)	5.68(61.48)	9.01(75.87)	10.49
PM (KL)	1.19(38.73)	1.75(56.07)	3.72(78.12)	4.93
PM (locΔRA950)	2.86(9.07)	4.38(33.94)	8.88(60.54)	11.48

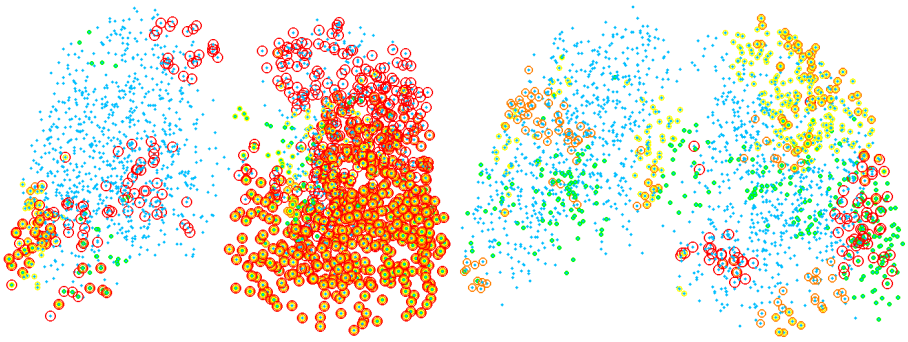

(a) (b)

Figure 7.2: All selected random samples marked in blue color. Locations with the significantly large dissimilarity measure obtained from the complete set of features at the 3, 12, 21, 30(24) months follow up visits are indicated in green, yellow, orange and red markers respectively.

Leibler divergence between local histograms of the smoothed images. The time trend was less significant for the measurement obtained from the complete set of dissimilarities. One of the possible explanations could be sensitivity of the particular dissimilarity measure to the change in image appearance not related to the emphysema progression, for example inflammation or change in local topology like collapsing or appearing bullae. Another possible explanation could be in the construction of the overall combined disease progression score from the complete vector of dissimilarities.

The current drawback of the proposed method is the simplification of the complete dissimilarity vector by its norm. The emphysema is usually characterized by the destruction of the lung tissue thus decreasing image intensities, while inflammation should result in increase of image intensities. In the current framework the two phenomena could result in equal dissimilarity measures. The specific dissimilarity measures such as difference in means of the local histograms is capable of differentiating between the two processes, therefore a careful investigation of the dissimilarity measures should be done. Furthermore an automatic

classification approach could be adapted for this problem, where samples from the image pairs with the 3 months follow up scan represent stable group while samples from the image pairs with the 30(24) months follow up scan represents the progressed group.

To conclude, we proposed a method for estimating local disease progression. Results suggested that emphysema progression can be detected before the tissue intensity decreases below the standard CT threshold of -950HU.

7.6 Appendix

This section presents four interesting cases in our dataset. For each case the figure displays snap shots of the baseline and the deformed follow up images and the table presets lung function test (FEV1), global emphysema index (RA950), and averaged local dissimilarity measures computed from the complete set of features (PM (all)); from Kullback-Leibler divergence of the smoothed image histograms (PM (KL)); and local emphysema index, (PM (locΔRA950)).

Each row in the top figure shows mean intensity projection over a stack of 9 sequential slices, uniformly sampled from the volumetric image. The left most column shows slices extracted from the baseline image, the remaining columns show corresponding slices extracted from the registered 3, 12, 21 and 30(24) months follow up visits, respectively from left to right. All the slices are displayed in the intensity range [-1000,-900]HU. In the bottom part of the figure, three plots show locations of all random samples (blue color) and locations that were marked as outliers based on the progression measure computed from the complete set of features (the left plot); from the Kullback-Leibler divergence of the smoothed image histograms (the middle plot); and from the local area below -950HU (the right plot). Locations marked as outliers in the 3, 12, 21 and 30(24) months follow ups are indicated in green, yellow, orange and red colors respectively.

Case A		3mnths	12mnths	21mnths	30(24)mnths
RA950	44.15	42.60	40.96	45.13	46.22
FEV1	1.41	1.50	1.57	1.44	1.36
PM (all)		0.96	1.10	1.13	1.47
PM (KL)		0.70	0.78	0.93	1.16
PM (locΔRA950)		-0.18	-0.62	0.45	0.91

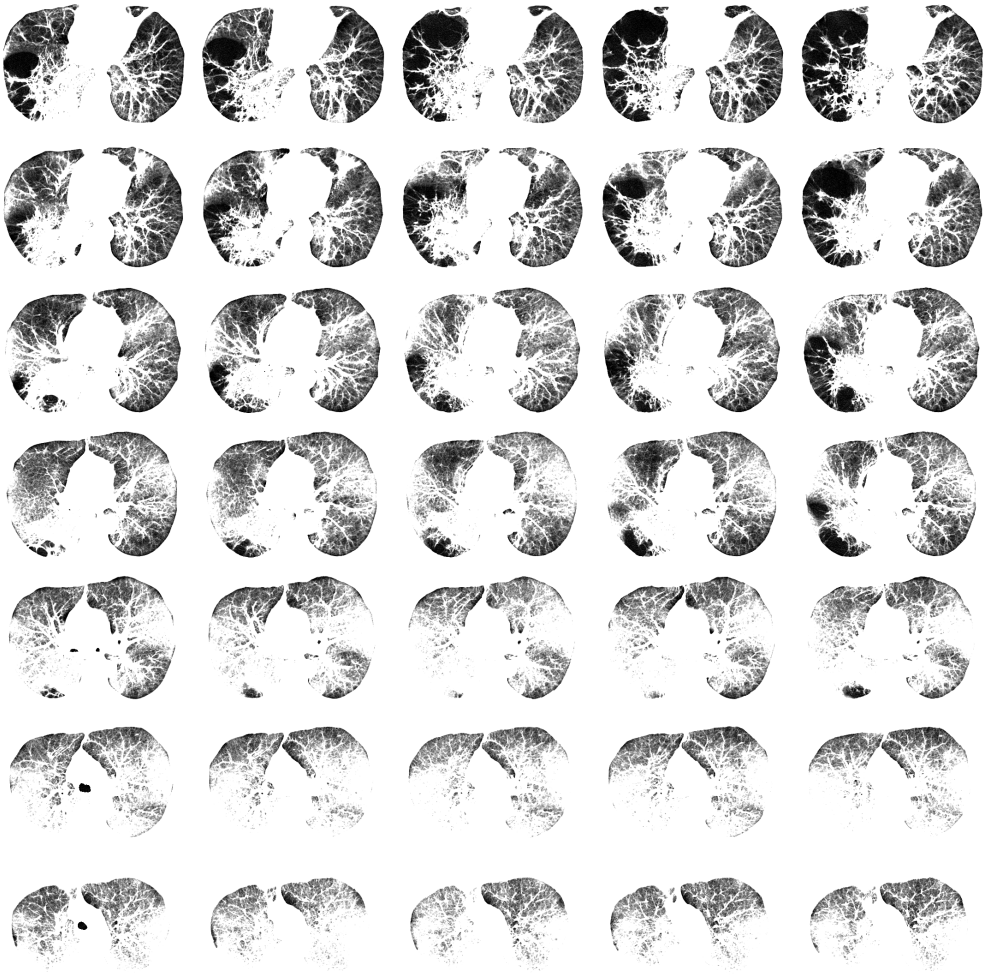

(a)

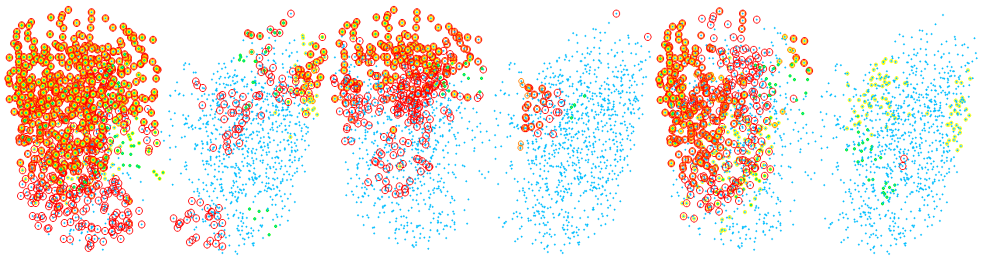

(b) (c) (d)

Case B		3mnths	12mnths	21mnths	30(24)mnths
RA950	40.52	34.24	36.80	37.90	43.69
FEV1	1.51	1.43	1.38	1.36	1.13
PM (all)		0.99	0.97	0.95	0.77
PM (KL)		0.67	0.75	0.82	0.89
PM (locΔRA950)		-1.18	-0.38	-0.27	0.43

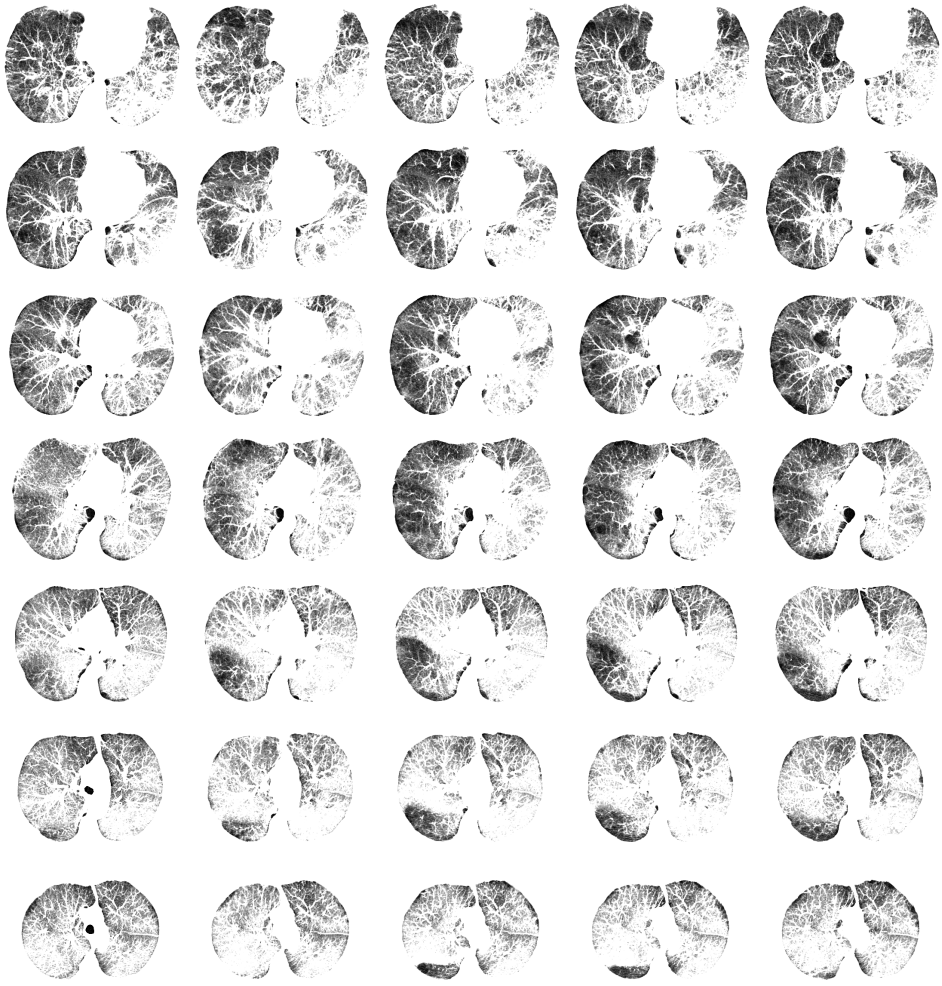

(a)

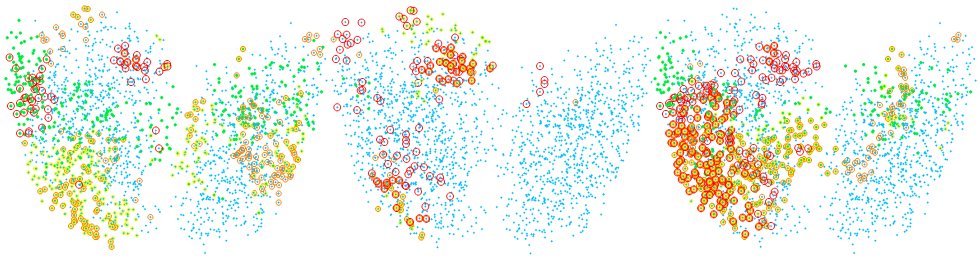

(b) (c) (d)

Case C		3mnths	12mnths	21mnths	30(24)mnths
RA950	62.00	59.82	61.57	70.50	69.94
FEV1	1.08	1.03	1.06	NA	NA
PM (all)		1.08	1.09	3.47	3.49
PM (KL)		0.84	0.92	1.60	1.64
PM (locΔRA950)		-0.04	0.40	2.73	2.95

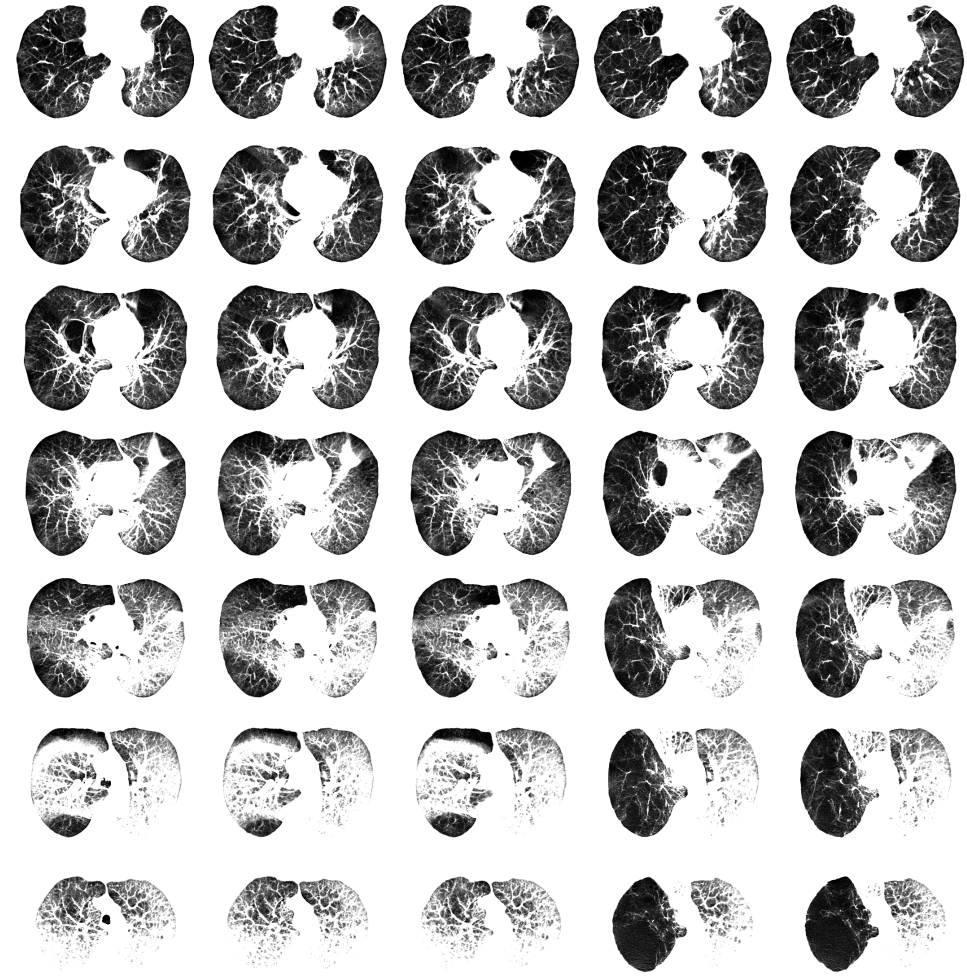

(a)

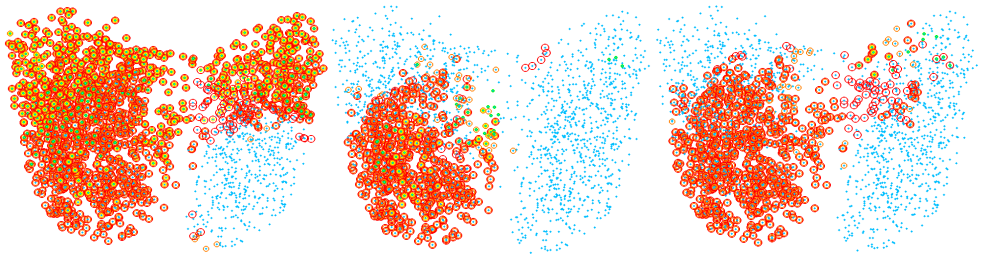

(b) (c) (d)

Case D		3mnths	12mnths	21mnths	30(24)mnths
RA950	28.33	24.46	30.30	30.92	31.29
FEV1	2.64	2.64	2.57	2.48	2.40
PM (all)		0.78	0.68	0.79	0.86
PM (KL)		0.46	0.60	0.61	0.66
PM (locΔRA950)		-0.73	1.04	1.16	1.42

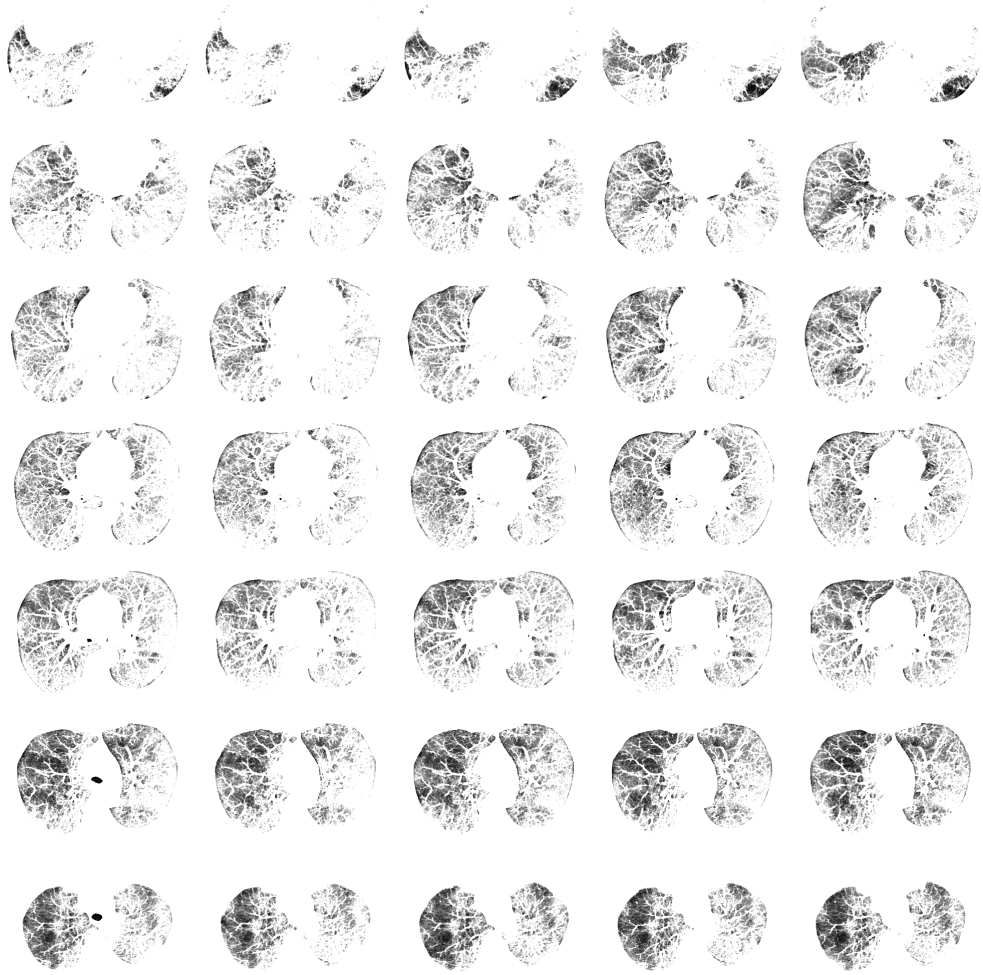

(a)

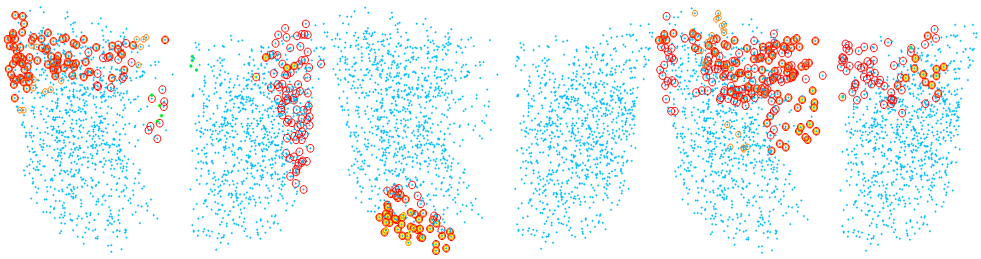

(b) (c) (d)

Chapter 8

Summary and Discussion

Science is always wrong. It never solves a problem without creating ten more.

— George Bernard Shaw

In this thesis, the problem of image registration for monitoring disease progression was investigated. Provided the point correspondence between the two longitudinal CT lung scans, the changes between the scans is revealed in the difference image. Image registration is a powerful tool and capable of establishing point correspondence with an accuracy of just 1 voxel. For monitoring disease progression such an accurate registration could be unfavourable, because then the deformed image will appear exactly the same as the fixed image and the difference between the two will be completely eliminated. An example illustrating the performance of the registration method was presented in the Chapter 1, where bulla expanded over the time and bullas borders was not matched. The change in bulla size was apparent in the difference image.

We started with a conventional image registration method, where multi-level B-Spline transform function and sum of squared differences dissimilarity function were used. The size of the B-Spline grids were conditioned upon the scale of lung lobes, segments and sub-segments. Human lungs contains 5 lobes and 18 lung segments. With an average lung volume of 5 liters, the linear scale of a lung lobe is approximately 10 cm and the linear scale of a lung segment is approximately 6.5 cm. We wanted to establish an accurate correspondence but not to overfit the images and eliminate the difference between the two images, thus size of the smallest B-Spline grid was about 2.5 cm. Whereas size of the smallest B-Spline

grid in our registration algorithm was generally larger than the size used in other B-Spline-based registration algorithms, the accuracy of the proposed registration method was comparable with the existing registration algorithms. Authors in [38, 50, 109] reported the size of the smallest B-Spline grid of approximately 8 voxels; K. Murphy et al. [78] reported 10 mm; Z. Wu et al. [48] reported the size of 50 mm.

Registration of lung CT scans is a complex problem, because lung appearance significantly depends on the inspiration level. Although subjects in this study were scanned at the maximum inspiration level, the variation in lung volume between the longitudinal scans was up to one liter leading to the complex and non-homogeneous deformations of lungs. Additional inspiration resulted in lower intensities of lung parenchyma in CT scans. This could be confused with the emphysema progression since emphysema is a destruction of lung tissue and also results in intensity decrease of lung parenchyma. The change in inspiration affects all the conventional densitometric measurements, e.g., relative area below 950HU, 15th percentile density and average lung density thus making it unreliable measures of emphysema progression. We proposed a novel solution - the mass preserving model of lungs, where lung density is inversely proportional to the local volume change in lungs. This model allows to compensate the regional change in intensity related to the regional change in the inspiration level. In Chapter 2 we investigated the mass preserving model and showed that incorporation mass preserving model directly into the image registration improves registration accuracy. Recently, the mass preserving model of lungs was also studied by other research groups and also showed better registration accuracy and more feasible deformations of lungs [38, 116, 56, 107]. The recent study [107] showed correlation of 0.9 between the lung ventilation estimated from the Xe-CT images and estimated from the mass preserving image registration. The mass preserving model was successfully applied in pilot experiments on monitoring emphysema progression presented in the Chapter 6 and in [31].

After spending numerous hours looking at the registration results, I was convinced that intensity-based registration could not register peripheral area accurately. Therefore we developed a feature-based algorithm dedicated to match vessels centerlines in Chapter 3. The algorithm was based on the existing current-based registration where no point correspondence was required. Question of how to combine information from the current-based registration in Chapter 3 and the intensity-based registration in Chapter 2 was addressed in Chapter 4. We proposed a novel registration method, where intensity-based registration was constrained with the deformations of the vessel centerlines obtained from the current-based registration. The important result was that by incorporating information from the feature-based registration into the intensity-based registration we were able to improve the accuracy of the registration using the same transformation

model. The recent study [107] showed that incorporating dissimilarity between vesselness filter responses along with the dissimilarity between the original images significantly improves registration accuracy. The downside of the proposed approach was its computational complexity. Therefore we returned to the image registration method from Chapter 2 in the following experiments.

Finally, we revisited the emphysema progression problem and this time we developed a framework which compensates for small mis-registrations. Alignment of longitudinal images was a first step towards analysis of regional emphysema progression. Although image registration provides point-to-point correspondence with accuracy of few millimeters, the direct point-to-point comparison of lung CT images has critical drawbacks. First, intensity of lung CT image only partially related to the true density of the tissue, because of the noise and partial volume effect. Secondly, different regions in lungs are registered with different accuracy, therefore in regions with lower registration accuracy direct point-to-point comparison is affected more by mis-registrations. Instead of the direct point-to-point comparison of image intensities, we proposed to adapt the concept of locally orderless images. Local image histograms at the corresponding locations in the baseline and deformed follow up images were compared by means of several dissimilarity measures. Along with the original images, we computed local histograms from the filtered versions of the images, e.g., gaussian blur and gradient magnitude filters. Dissimilarity measures included both distance measure between histograms and differences in individual measurements, e.g., moments of histograms. This framework is both robust to noise presented in the images and to small mis-registrations. Experiments showed promising results however more detailed investigation should be performed.

To conclude, four main contributions were made in this thesis:

- mass preserving registration was proposed and justified on a large amount of data;
- current-based registration framework was adapted for registering lung CT scans;
- combined feature-based and intensity-based registration method was proposed and validated via manually annotated landmarks;
- framework for monitoring emphysema progression was developed and tested on patients with Alpha-1 Antitrypsin Deficiency.

8.1 Discussion

The proposed mass preserving model is a simple model, where density of lung tissue is assumed to be inverse proportionally to the volume. With the mass

preserving model, intensities are linearly transformed with the fixed point at the intensity of air, -1000HU. Generally, if we observe uniform expansion of lungs, we believe that for lung parechyma mass preservation is correct, but for expanding vessel the mass preservation is not applicable. If a vessel expands/contracts intensity or density should remain constant. This leads to a second fixed point in the intensity adjustment model at 0 HU. Since there is no linear intensity adjustment model with two fixed points, e.g., at the value -1000HU and 0HU, the intensity adjustment should be applied locally only for voxels from lung parenchyma.

If an image registration algorithm provides feasible deformations of lungs caused by additional inspiration, the mass preserving model will then compensate lung tissue density change imposed by the deformations. The physiologically correct and plausible deformations are critical issues for the mass preserving lung model. Recent study by Kabus S. et al. [24], compared deformation fields of several registration algorithms. Even with comparable registration accuracy, different algorithms resulted in significantly different deformation fields. Therefore a thorough inspection of the deformation field is needed before applying mass preserving intensity correction.

Another question that should be investigated is the range of lung volume changes where mass preservation holds. For example, during tidal breathing the range of possible lung volumes is significantly smaller than variations in lung volume from maximum expiration to maximum inspiration. In those extreme cases preservation of lung mass may not hold. Another case when inflammation is observed only in one of the scans, the mass preserving model of lungs does not hold. In those cases a more advanced model of lungs should be developed.

An interesting research topic addressed in this thesis was the problem of monitoring disease progression. With the proposed local image comparison framework several questions could be further investigated, e.g., how the emphysema progression in a region affects the surrounding regions and how we could predict disease development.

An interesting question that could be investigated in the future, is local analysis of deformation fields. Assuming that registration provides physiologically correct deformations of lungs, one could investigate if there is a difference in the deformations of healthy and diseased tissues. Since emphysema is characterized by decrease of lung tissue elasticity this phenomena may be reflected in the deformation fields.

Several research questions emerged along the past three years were not investigated in the thesis. With the rapidly increasing number of longitudinal lung CT studies and many research groups working on the topic, those questions definitely will be solved in foreseeable future.

List Of Publications

Papers in peer-reviewed conferences

- Gorbunova V., Lo P., Ashraf H., Dirksen A., Nielsen M., de Bruijne M., "Weight Preserving Image Registration for Monitoring Disease Progression in Lung CT" in *Medical Image Computing and Computer Assisted Intervention Conference*, 2008.
- Gorbunova V., Lo P., Loeve M., Tiddens H., Sporring J., Nielsen M., de Bruijne M., "Mass Preserving Registration for Lung CT" in *SPIE Medical Imaging*, 2009.
- Gorbunova V., Durrleman S., Lo P., Pennec X., de Bruijne M., "Lung CT Registration Combining Intensity, Curves and Surfaces" in *IEEE International Symposium on Biomedical Imaging*, 2010.
- Gorbunova V., Jacobs S.A.M., Lo P., Dirksen A., Nielsen M., Bab-Hadiashar A., de Bruijne M., "Early Detection of Emphysema Progression" to appear in *Medical Image Computing and Computer Assisted Intervention Conference*, 2010.

Papers in peer-reviewed workshops

- Gorbunova V., Durrleman S., Lo P., Pennec X., de Bruijne M., "Curve- and Surface-based registration of lung CT images via currents" in *Second International Workshop on Pulmonary Image Analysis*, 2009.
- Gorbunova V., Sporring J., Lo P., Dirksen A., de Bruijne M., "Mass Preserving Registration for lung CT: EMPIRE10 Challenge Results" to appear in *Grand Challenges in Medical Image Analysis Workshop*, 2010.

Bibliography

[1] Wilhelm Conrad Röntgen. Über eine neue art von strahlen. *Aus den Sitzungberichten der Würzburger Physik.-medic. Gesellschaft*, 1895. [cited at p. 1]

[2] R Green. Fleischner Lecture. Imaging the respiratory system in the first few years after discovery of the X-ray: contributions of Francis H. Williams, M.D. *American Journal of Roentgenology*, 159:1–7, 1992. [cited at p. 2]

[3] A Vallebona. Radiography with great enlargement (micro-radiography) and a technical method for the radiographic dissociation of the shadow. *Radiology*, 17:340–341, 1931. [cited at p. 2]

[4] G N Hounsfield. Computerized transverse axial scanning (tomography): Part1. description of system. *British Journal of Radiology*, 46:1016–1022, 1973. [cited at p. 2]

[5] K.F. Rabe et al. Global strategy for the diagnosis, management, and prevention of chronic obstructive pulmonary disease gold executive summary. *American Journal of Respiratory and Critical Care Medicine*, 176:532–555, 2007. [cited at p. 5, 22, 73, 76, 81]

[6] World health statistics. Technical report, 2008. [cited at p. 5]

[7] A Dirksen, F Rasmussen, and N Keiding. Choice of measurement and sample size for detection of changes in lung function in obstructive pulmonary disease. *European Respiratory Review*, 5:432–435, 1991. [cited at p. 5]

[8] Asger Dirksen, NH Holstein-Rathlou, F Madsen, LT Skovgaard, CS Ulrik, T Heckscher, and A Kok-Jensen. Long-range correlations of serial FEV_1 measurements in emphysematous patients and normal subjects. *The Americca Physiological Society*, 85:259–265, 1998. [cited at p. 5]

[9] JW Gurney, KK Jones, RA Robbins, GL Gossman, KJ Nelson, D Daughton, JR Spurzem, and SI Rennard. Regional distribution of emphysema: correlation of high-resolution ct with pulmonary function tests in unselected smokers. *Radiology*, 183:182–185, 1992. [cited at p. 5]

[10] JS Klein, G Gamsu, WR Webb, JA Golden, and NL Muller. High-resolution ct diagnosis of emphysema in symptomatic patients with normal chest radiographs and isolated low diffusing capacity. *Radiology*, 182:817–821, 1992. [cited at p. 5]

[11] Naidich D.P Webb R.W., Muller N. L. *High-Resolution CT of the Lung*. Lippincott Williams and Wilkins, 2001. [cited at p. 5]

[12] M. Els Bakker, Hein Putter, Jan Stolk, Saher B Shaker, Eeva Piitulainen, Erich W Russi, and Berend C Stoel. Assessment of regional progression of pulmonary emphysema with CT densitometry. *CHEST*, 134(5):931–937, Nov 2008. [cited at p. 5, 6]

[13] E. A. Hoffman, J. M. Reinhardt, M. Sonka, B. A. Simon, J. Guo, O. Saba, D. Chon, S. Samrah, H. Shikata, J. Tschirren, K. Palagyi, K. C. Beck, and G. McLennan. Characterization of the Interstitial Lung Diseases via Density-Based and Texture-Based Analysis of Computed Tomography Images of Lung Structure and Function. *Academic Radiology*, 10(10):1104–1118, 2003. [cited at p. 5]

[14] J Stolk et al. Progression parameters for emphysema: a clinical investigation. *Respiratory Medicine*, 101(9):1924–30, 2007. [cited at p. 5, 78]

[15] J Zaporozhan et al. Paired inspiratory/expiratory volumetric thin-slice CT scan for emphysema analysis: Comparison of different quantitative evaluations and pulmonary function test. *CHEST*, 128:3212–3220, 2005. [cited at p. 5]

[16] A. Dirksen, E. Piitulainen, D.G. Parr, C. Deng, M. Wencker, and S.B. Shakerand R.A. Stockley. Exploring the role of CT densitometry: a randomised study of augmented therapy in α_1-antitrypsin deficiency. *European Respiratory Journal*, 33:1345–1353, 2009. [cited at p. 5, 6, 14, 81, 82]

[17] H.A. Gietema, A.M. Schilham, B. van Ginneken, R.J. van Klaveren, J.W.J. Lammers, and M. Prokop. Monitoring of smoking-induced emphysema with CT in a lung cancer screening setting: Detection of real increase in extent of emphysema. *Radiology*, 244, 3:890–897, 2007. [cited at p. 5, 74, 81]

[18] David G Parr, Martin Sevenoaks, Chunqin Deng, Berend C Stoel, and Robert A Stockley. Detection of emphysema progression in alpha 1-

antitrypsin deficiency using CT densitometry; methodological advances. *Respiratory Research*, 9:21, 2008. [cited at p. 5]

[19] E.M. van Rikxoort, M. Prokop, B. de Hoop, M.A. Viergever, J.P.W. Pluim, and B. van Ginneken. Automatic segmentation of the pulmonary lobes from fissures, airways, and lung borders: evaluation of robustness against missing data. *Proc. Medical Image Computing and Computer Assisted Intervention (MICCAI)*, 5761:263–271, 2009. [cited at p. 6]

[20] Li Zhang, Eric A Hoffman, and Joseph M Reinhardt. Atlas-driven lung lobe segmentation in volumetric X-ray CT images. *IEEE Transactions on Medical Imaging*, 25(1):1–16, 2006. [cited at p. 6, 16]

[21] Jan-Martin Kuhnigk, Volker Dicken, Stephan Zidowitz, Lars Bornemann, Bernd Kuemmerlen, Stefan Krass, Heinz-Otto Peitgen, Silja Yuval, Hans-Holger Jend, Wigbert S. Rau, and Tobias Achenbach. New Tools for Computer Assistance in Thoracic CT. Part 1. Functional Analysis of Lungs, Lung Lobes, and Bronchopulmonary Segments. *Radiographics*, 25:525–536, 2005. [cited at p. 6]

[22] E.M. van Rikxoort, B. de Hoop, S. van de Vorst, M. Prokop, and B. van Ginneken. Automatic segmentation of pulmonary segments from volumetric chest CT scans. *IEEE Transactions on Medical Imaging*, 28(4):621–630, 2009. [cited at p. 6]

[23] K. Murphy, B. van Ginneken, J.P.W. Pluim, S. Klein, and M. Staring. Semi-automatic reference standard construction for quantitative evaluation of lung CT registration. In Dimitris Metaxas, Leon Axel, Gábor Székely, and Gabor Fichtinger, editors, *Proc. Medical Image Computing and Computer Assisted Intervention (MICCAI)*, volume 5242 of *Lecture Notes in Computer Science*, pages 1006–1013, 2008. [cited at p. 6, 11, 12, 18, 31, 65]

[24] Sven Kabus, Tobias Klinder, Keelin Murphy, Bram van Ginneken, Cristian Lorenz, and Josien P. W. Pluim. Evaluation of 4D-CT lung registration. In Guang-Zhong Yang, David J. Hawkes, Daniel Rueckert, J. Alison Noble, and Chris J. Taylor 0002, editors, *Proc. Medical Image Computing and Computer Assisted Intervention (MICCAI)*, volume 5761 of *Lecture Notes in Computer Science*, pages 747–754. Springer, 2009. [cited at p. 6, 48, 98]

[25] Margrit Betke, Harrison Hong, Deborah Thomas, Chekema Prince, and Jane P Ko. Landmark detection in the chest and registration of lung surfaces with an application to nodule registration. *Medical Image Analysis*, 7(3):265–281, 2003. [cited at p. 7, 11, 31, 36, 48]

[26] Helen Hong, Jeongjin Lee, and Yeny Yim. Automatic lung nodule matching on sequential CT images. *Computers in Biology and Medicine*, 38(5):623–634, 2008. [cited at p. 7, 16]

[27] Yuanjie Zheng, K. Steiner, T. Bauer, Jingyi Yu, Dinggang Shen, and C. Kambhamettu. Lung nodule growth analysis from 3D CT data with a coupled segmentation and registration framework. In *IEEE 11th International Conference on Computer Vision*, pages 1–8, Oct 2007. [cited at p. 7, 16]

[28] Y. Arzhaeva, M. Prokop, K. Murphy, E.M. van Rikxoort, P.A. de Jong, H.A. Gietema, M.A. Viergever, and B. van Ginneken. Automated estimation of progression of interstitial lung disease in CT images. *Medical Physics*, 37(1):63–73, 2010. [cited at p. 7, 48]

[29] Vladlena Gorbunova, Pechin Lo, Haseem Ashraf, Asger Dirksen, Mads Nielsen, and Marleen de Bruijne. Weight preserving image registration for monitoring disease progression in lung CT. In Dimitris Metaxas, Leon Axel, Gábor Székely, and Gabor Fichtinger, editors, *Proc. Medical Image Computing and Computer Assisted Intervention (MICCAI)*, volume 5242 of *Lecture Notes in Computer Science*, pages 863–870, 2008. [cited at p. 8, 12, 16, 17, 29, 40, 48, 82]

[30] Vladlena Gorbunova, Sanders S.A.M. Jacobs, Lo Pechin, Asger Dirksen, Mads Nielsen, Alireza Bab-Hadiashar, and Marleen de Bruijne. Early detection of emphysema progresison. In *Proc. Medical Image Computing and Computer Assisted Intervention (MICCAI)*, Lecture Notes in Computer Science, 2010. [cited at p. 8]

[31] Marius Staring, M.E. Bakker, D.P. Shamonin, J. Stolk, J.H.C. Reiber, and B.C. Stoel. Towards local estimation of emphysema progression using image registration. In J.P.W. Pluim and B.M. Dawant, editors, *SPIE (Medical Imaging)*, volume 7259 of *Proceedings of SPIE*, Feb 2009. [cited at p. 8, 16, 29, 82, 96]

[32] Jan Modersitzki. *Numerical Methods for Image Registration*. Oxford University Press, 2004. [cited at p. 8, 9]

[33] Milan Sonka and J. Michael Fitzpatrick. *Handbook of Medical Imaging*, volume 20. 2001. [cited at p. 8]

[34] Vlad Boldea, David Sarrut, and S. C. Lung. Lung Deformation Estimation with Non-Rigid Registration for Radiotherapy Treatment. In *Proc. Medical Image Computing and Computer Assisted Intervention (MICCAI)*, volume

2878 of *Lecture Notes in Computer Science*, pages 770–777. Springer Verlag, R.E. Ellis and T.M. Peters, 2003. MICCAI 2003. [cited at p. 9]

[35] K. Ding, J.E. Bayouth, J.M. Buatti, G.E. Christensen, and J.M. Reinhardt. 4D CT-based measurement of changes in pulmonary function following a course of radiation therapy. *Medical Physics*, 37(3):1261–72, 2010. [cited at p. 9, 16]

[36] D Mattes, D Haynor, H Vesselle, T Lewellen, and W Eubank. PET-CT image registration in the chest using free-form deformations. *IEEE Transactions on Medical Imaging*, 22:120–128, 2003. [cited at p. 9, 12, 17, 48, 76]

[37] Torbjorn Vik, Sven Kabus, Jens von Berg, Konstantin Ens, Sebastian Dries, Tobias Klinder, and Cristian Lorenz. Validation and comparison of registration methods for free-breathing 4D lung-CT. In J. M. Reinhardt and J. P. W. Pluim, editors, *SPIE (Medical Imaging)*, volume 6914, 2008. [cited at p. 9, 12, 30, 36, 48]

[38] Youbing Yin, Eric A. Hoffman, and Ching-Long Lin. Mass preserving nonrigid registration of CT lung images using cubic B-spline. *Medical Physics*, 36(9):4213–4222, 2009. [cited at p. 9, 12, 17, 30, 96]

[39] Richard Castillo, Edward Castillo, Rudy Guerra, Valen E Johnson, Travis McPhail, Amit K Garg, and Thomas Guerrero. A framework for evaluation of deformable image registration spatial accuracy using large landmark point sets. *Physics in Medicine and Biology*, 54(7):1849–1870, 2009. [cited at p. 9, 11, 14, 24, 25, 30, 39, 48, 49, 53, 56]

[40] Baojun Li, Gary E. Christensen, Eric A. Hoffman, Geoffrey McLennan, and Joseph M. Reinhardt. Pulmonary CT image registration and warping for tracking tissue deformation during the respiratory cycle through 3D consistent image registration. *Medical Physics*, 35(12):5575–5583, 2008. [cited at p. 9]

[41] Deshan Yang, Wei Lu, Daniel A. Low, Joseph O. Deasy, Andrew J. Hope, and Issam El Naqa. 4D-CT motion estimation using deformable image registration and 5D respiratory motion modeling. *Medical Physics*, 35(10):4577–4590, 2008. [cited at p. 9]

[42] Thomas Guerrero, Kevin Sanders, Edward Castillo, Yin Zhang, Luc Bidaut, Tinsu Pan, and Ritsuko Komaki. Dynamic ventilation imaging from four-dimensional computed tomography. *Physics in Medicine and Biology*, 51(4):777–791, Feb 2006. [cited at p. 9, 16]

[43] J B A Maintz and M Z Viergever. A survey of medical image registration. *Medical Image Analysis*, 2:1–37, 1998. [cited at p. 11]

[44] K. Rohr, H. S. Stiehl, R. Sprengel, T. M. Buzug, J. Weese, and M. H. Kuhn. Landmark-based elastic registration using approximating thin-plate splines. *IEEE Transactions on Medical Imaging*, 20(6):526–534, 2001. [cited at p. 12, 36, 48]

[45] Sven Kabus, Jens von Berg, Tokihiro Yamamoto, Roland Opfer, and Paul J. Keall. Lung ventilation estimation based on 4D-CT imaging. In M. Brown, M. de Bruijne, B. van Ginneken, A. Kiraly, J.M. Kuhnigk, C. Lorenz, K. Mori, and J. Reinhardt, editors, *First International Workshop on Pulmonary Image Analysis*, pages 73–83, 2008. [cited at p. 12, 16]

[46] Vladlena Gorbunova, Stanley Durrleman, Pechin Lo, Xavier Pennec, and M de Bruijne. Curve- and surface-based registration of lung CT images via currents. In *Second International Workshop on Pulmonary Image Analysis*, 2009. [cited at p. 12, 48, 50]

[47] M. Hub, M. L. Kessler, and C. P. Karger. A stochastic approach to estimate the uncertainty involved in b-spline image registration. *IEEE Transactions on Medical Imaging*, 28:1708 – 1716, 2009. [cited at p. 12, 19, 57]

[48] Ziji Wu, Eike Rietzel, Vlad Boldea, David Sarrut, and Gregory C Sharp. Evaluation of deformable registration of patient lung 4DCT with subanatomical region segmentations. *Medical Physics*, 35(2):775–781, Feb 2008. [cited at p. 12, 16, 18, 30, 48, 96]

[49] Vlad Boldea, Gregory C Sharp, Steve B Jiang, and David Sarrut. 4D-CT lung motion estimation with deformable registration: quantification of motion nonlinearity and hysteresis. *Medical Physics*, 35(3):1008–1018, Mar 2008. [cited at p. 12, 16]

[50] Marius Staring, Stefan Klein, and Josien P.W. Pluim. A rigidity penalty term for nonrigid registration. *Medical Physics*, 34(11):4098 – 4108, Nov 2007. [cited at p. 12, 16, 96]

[51] Stefan Klein, Marius Staring, and Josien P W Pluim. Evaluation of optimization methods for nonrigid medical image registration using mutual information and B-splines. *IEEE Transactions on Image Processing*, 16(12):2879–2890, Dec 2007. [cited at p. 12, 19, 21, 55]

[52] Joseph M Reinhardt, Kai Ding, Kunlin Cao, Gary E Christensen, Eric A Hoffman, and Shalmali V Bodas. Registration-based estimates of local lung tissue expansion compared to xenon CT measures of specific ventilation. *Medical Image Analysis*, 12(6):752–763, Dec 2008. [cited at p. 12, 16, 17, 48]

[53] Gary E. Christensen, Joo Hyun Song, Wei Lu, Issam El Naqa, and Daniel A. Low. Tracking lung tissue motion and expansion/compression with inverse

consistent image registration and spirometry. *Medical Physics*, 34(6):2155–2164, 2007. [cited at p. 12, 16, 47, 48, 74]

[54] Hiroaki Arakawa, Pierre Alain Gevenois, Yoshiaki Saito, Hisao Shida, Viviane De Maertelaer, Hiroshi Morikubo, and Mutsuhisa Fujioka. Silicosis: expiratory thin-section CT assessment of airway obstruction. *Radiology*, 236(3):1059–1066, Sep 2005. [cited at p. 12]

[55] Thomas Guerrero, Geoffrey Zhang, William Segars, Tzeng-Chi Huang, Stephen Bilton, Geoffrey Ibbott, Lei Dong, Kenneth Forster, and Kang Ping Lin. Elastic image mapping for 4-D dose estimation in thoracic radiotherapy. *Radiation Protection Dosimetry*, 115:497–502, 2005. [cited at p. 12, 16]

[56] Edward Castillo, Richard Castillo, Yin Zhang, and Thomas Guerrero. Compressible image registration for thoracic computed tomography images. *Journal of Medical and Biological Engineering*, 29:236–247, 2009. [cited at p. 12, 17, 30, 60, 96]

[57] J.W. Suh, D. Scheinost, X. Qian, A.J. Sinusas, C.K. Breuer, and X. Papademetris. Serial nonrigid vascular registration using weighted normalized mutual information. In *IEEE International Symposium on Biomedial Imaging*, 2010. [cited at p. 12]

[58] Tianming Liu, Dinggang Shen, and Christos Davatzikos. Deformable registration of cortical structures via hybrid volumetric and surface warping. *NeuroImage*, 22(4):1790 – 1801, 2004. [cited at p. 12, 49]

[59] Han Jingfeng, Hornegger Joachim, Kuwert Torsten, Bautz Werner, and Romer Wolfgang. Feature constrained non-rigid image registration. In *18th Symposium on Simulationstechnique*, 2005. [cited at p. 12, 49]

[60] Vladlena Gorbunova, Stanley Durrleman, Pechin Lo, Xavier Pennec, and Marleen de Bruijne. Lung CT registration combining intensity, curves and surfaces. In *IEEE International Symposium on Biomedial Imaging*, pages 340–343, 2010. [cited at p. 12, 48, 49]

[61] D. Rueckert, L. I. Sonoda, C. Hayes, D. L. G. Hill, M. O. Leach, and D. J. Hawkes. Nonrigid registration using free-form deformations: Application to breast MR images. *IEEE Transactions on Medical Imaging*, 18:712–722, 1999. [cited at p. 12, 17, 48, 50]

[62] G. Christensen, R. D. Rabitt, and M. I. Miller. Deformable templates using large deformation kinematics. *IEEE Transactions on Medical Imaging*, 5:1435–1447, 1996. [cited at p. 12, 48]

[63] Morten Bro-Nielsen. *Medical Image Registration and Surgery Simulation.* PhD thesis, Technical University of Denmark, Department of Mathematical Modelling, 1996. [cited at p. 12]

[64] C Briot. *Optimal Registration of Deformed Images.* PhD thesis, University of Pennsylvania, Philadelphia, 1981. [cited at p. 12]

[65] Ruzena Bajcsy and Stanislav Kovacic. Multiresolution elastic matching. *Computer Vision, Graphics, and Image Processing*, 46(1):1–21, 1989. [cited at p. 12]

[66] Berthold K. P. Horn and Brian G. Schunk. Determining optical flow. *Artificial Intelligence*, 17:185–203, 1981. [cited at p. 12]

[67] Jesper Pedersen, Haseem Ashraf, Asger Dirksen, Karen Bach, Hanne Hansen, Phillip Toennesen, Hanne Thorsen, John Brodersen, Birgit Skov, Martin Døssing, Jann Mortensen, Klaus Richter, Paul Clementsen, and Niels Seersholm. The Danish randomized lung cancer CT screening trial - overall design and results of the prevalence round. *Journal of Thoracic Oncology*, 4:608–614, Apr 2009. [cited at p. 14, 24]

[68] PA de Jong, Y Nakano, MH Lequin, R Woods, RD Pare, and Hawm Tiddens. Progressive damage on high-resolution computed tomography despite stable lung function in CF. *European Respiratory Journal*, 23:93–97, 2004. [cited at p. 14, 25]

[69] ITK. *Insight Segmentation and Registration Toolkit, http://www.itk.org/.* [cited at p. 14, 76]

[70] David Tschumperle. *CImg C++ Template Image Processing Toolkit, http://cimg.sourceforge.net/.* [cited at p. 14]

[71] Stefan Klein and Marius Staring. *Elastix Toolkit, http://elastix.isi.uu.nl/index.php.* [cited at p. 14]

[72] S. Klein, M. Staring, K. Murphy, M. A. Viergever, and J. P.W. Pluim. elastix: a toolbox for intensity-based medical image registration. *IEEE Transactions on Medical Imaging*, 29(1):196–205, 2010. [cited at p. 14]

[73] Qianqian Fang. *A Matlab/Octave-based mesh generator. http://iso2mesh.sourceforge.net/cgi-bin/index.cgi.* [cited at p. 14, 37, 40, 54]

[74] I. Sluimer, A. Schilham, M. Prokop, and B. van Ginneken. Computer analysis of computed tomography scans of the lung: A survey. *IEEE Transactions on Medical Imaging*, 25:385–405, 2006. [cited at p. 15, 74]

[75] I.C. Sluimer, M. Prokop, and B. van Ginneken. Towards automated segmentation of the pathological lung in CT. *IEEE Transactions on Medical Imaging*, 24:1025–1038, 2005. [cited at p. 16]

[76] Pan Li, Urban Malsch, and Rolf Bendl. Combination of intensity-based image registration with 3D simulation in radiation therapy. *Physics in Medicine and Biology*, 53:4621–4637, 2008. [cited at p. 16, 36, 48, 49]

[77] Hidenori Ue, Hideaki Haneishi, Hideyuki Iwanaga, and Kazuyoshi Suga. Respiratory lung motion analysis using a nonlinear motion correction technique for respiratory-gated lung perfusion SPECT images. *Annals of Nuclear Medicine*, 21:175–183, 2007. [cited at p. 16]

[78] Keelin Murphy, Bram van Ginneken, Eva M. van Rixkoort, B J de Hoop, M Prokop, P Lo, Marleen de Bruijne, and J P W Pluim. Obstructive pulmonary function: Patient classiffication using 3D registration of inspiration and expiration CT images. In *Second International Workshop on Pulmonary Image Analysis*, 2009. [cited at p. 16, 96]

[79] D. L. Hill, P. G. Batchelor, M. Holden, and D. J. Hawkes. Medical image registration. *Physics in Medicine and Biology*, 46(3):R1–45, Mar 2001. [cited at p. 16]

[80] A Pevsner, B Davis, S Joshi, A Hertanto, J Mechalakos, E Yorke, K Rosenzweig, S Nehmeh, YE Erdi, JL Humm, S Larson, CC Ling, and GS Mageras. Evaluation of an automated deformable image matching method for quantifying lung motion in respiration-correlated CT images. *Medical Physics*, 33:369–376, 2006. [cited at p. 16, 30]

[81] David Sarrut, Vlad Boldea, Serge Miguet, and C Ginestet. Simulation of 4D-CT Images from Deformable Registration between Inhale and Exhale Breath-hold CT Scans. *Medical Physics*, 33(3):605–617, March 2006. [cited at p. 16, 17, 48]

[82] S B Shaker, A Dirksen, L C Laursen, L T Skovgaard, and N H Holstein-Rathlou. Volume adjustment of lung density by computed tomography scans in patients with emphysema. *Acta Radiologica*, 4, 2004. [cited at p. 16, 74]

[83] Brett Simon. Non-invasive imaging of regional lung function using X-ray computed tomography. *Journal of Clinical Monitoring and Computing*, 16:433–442, 2000. [cited at p. 16]

[84] Lei Zhu, Yan Yang, Steven Haker, and Allen Tannenbaum. An image morphing technique based on optimal mass preserving mapping. *IEEE Transactions on Image Processing*, 16:1481–1495, 2007. [cited at p. 17]

[85] Youbing Yin, Eric Hoffman, and Ching-Long Lin. Local tissue-weight-based nonrigid registration of lung images with application to regional ventilation. In J.P.W. Pluim and B.M. Dawant, editors, *SPIE (Medical Imaging)*, volume 7262 of *Proc. SPIE*, 2009. [cited at p. 17]

[86] Vladlena Gorbunova, Pechin Lo, Martine Loeve, Harm Tiddens, Jon Sporring, Mads Nielsen, and Marleen de Bruijne. Mass preserving registration for lung CT. In J.P.W. Pluim and B.M. Dawant, editors, *SPIE (Medical Imaging)*, volume 7259 of *Proc. SPIE*, Feb 2009. [cited at p. 17]

[87] Pechin Lo, J Sporring, H Ashraf, J.J.H Pedersen, and M de Bruijne. Vessel-guided airway segmentation based on voxel classification. In *First International Workshop on Pulmonary Image Analysis*, 2008. [cited at p. 18, 20, 21, 37, 38, 40, 54]

[88] Daniel Rueckert, Paul Aljabar, Rolf A. Heckemann, Joseph V. Hajnal, and Alexander Hammers. Diffeomorphic registration using b-splines. In R. Larsen, M. Nielsen, and J. Sporring, editors, *Proc. Medical Image Computing and Computer Assisted Intervention (MICCAI)*, volume 2, pages 702–709, 2006. [cited at p. 18]

[89] T Wang and A Basu. A note on a fully parallel 3D thinning algorithm and its applications. *Pattern Recognition Letters*, 28(4):501–506, 2007. [cited at p. 20, 38, 54]

[90] H. J. Johnson and G. E. Christensen. Consistent landmark and intensity-based image registration. *IEEE Transactions on Medical Imaging*, 21:450–461, 2002. [cited at p. 36, 49]

[91] Fred L. Bookstein. *Morphological tools for landmark data; geometry and biology*. Cambridge University press, 1991. [cited at p. 36]

[92] S. C. Joshi and M. I Miller. Landmark matching via large deformation diffeomorphisms. *IEEE Transactions on Medical Imaging*, 9:1357–1370, 2000. [cited at p. 36, 39]

[93] Marc Vaillant and Joan Glaunes. Surface matching via currents. *Information Processing in Medical Imaging, 19th International Conference*, 3565:381–392, 2005. [cited at p. 36, 37, 39, 48]

[94] Joan Glaunès, Anqi Qiu, Michael I. Miller, and Laurent Younes. Large deformation diffeomorphic metric curve mapping. *International Journal of Computer Vision*, 80(3):317–336, 2008. [cited at p. 36, 37, 39, 48, 50]

[95] Stanley Durrleman, Xavier Pennec, Alain Trouvé, and Nicholas Ayache. Measuring brain variability via sulcal lines registration: a diffeomorphic

approach. In *Proc. Medical Image Computing and Computer Assisted Intervention (MICCAI)*, volume 4791 of *LNCS*, pages 675–682, 2007. [cited at p. 36]

[96] Stanley Durrleman, Xavier Pennec, Alain Trouvé, and Nicholas Ayache. Sparse approximation of currents for statistics on curves and surfaces. In *Proc. Medical Image Computing and Computer Assisted Intervention (MICCAI)*, volume 5242 of *LNCS*, pages 390–398, 2008. [cited at p. 36]

[97] Stanley Durrleman, Xavier Pennec, Alain Trouvé, Paul Thompson, and Nicholas Ayache. Inferring brain variability from diffeomorphic deformations of currents: an integrative approach. *Medical Image Analysis*, 12(5):626–637, 2008. [cited at p. 36, 37, 39, 48, 50]

[98] Stanley Durrleman and et al. Sparse approximation of currents for statistics on curves and surfaces. In *Proc. Medical Image Computing and Computer Assisted Intervention (MICCAI)*, volume 5242 of *LNCS*, pages 390–398, 2008. [cited at p. 36]

[99] Mutsumi Tashiro, Shinichi Minohara, Tatsuaki Kanai, Ken Yusa, Hideyuki Sakurai, and Takashi Nakano. Three-dimensional velocity mapping of lung motion using vessel bifurcation pattern matching. *Medical Physics*, 33(6):1747–1757, Jun 2006. [cited at p. 48]

[100] Pierre Hellier and Christian Barillot. Coupling dense and landmark-based approaches for non rigid registration. *IEEE Transactions on Medical Imaging*, 22:217–227, 2000. [cited at p. 48, 49]

[101] Dinggang Shen and Christos Davatzikos. Hammer: Hierarchical attribute matching mechanism for elastic registration. *IEEE Transactions on Medical Imaging*, 21:1421–1439, 2002. [cited at p. 49]

[102] Stephen R. Aylward, Julien Jomier, Sue Weeks, and Elizabeth Bullitt. Registration and analysis of vascular images. *International Journal of Computer Vision*, 55:123–138, 2004. [cited at p. 49]

[103] Charles V. Stewart, Ying-Lin Lee, and Chia-Ling Tsai. An uncertainty-driven hybrid of intensity-based and feature-based registration with application to retinal and lung ct images. In Christian Barillot, David R. Haynor, and Pierre Hellier, editors, *Proc. Medical Image Computing and Computer Assisted Intervention (MICCAI)*, volume 3216 of *Lecture Notes in Computer Science*. Springer, 2004. [cited at p. 49]

[104] K. Rohr, P. Cathier, and S. Wrz. Elastic registration of electrophoresis images using intensity information and point landmarks. *Pattern Recognition*, 37(5):1035 – 1048, 2004. [cited at p. 49]

[105] Pascal Cachier, Jean-Francois Mangin, Xavier Pennec, Denis Rivière, Dimitri Papadopoulos-Orfanos, Jean Régis, and Nicholas Ayache. Multisubject Non-rigid Registration of Brain MRI Using Intensity and Geometric Features. In Wiro J. Niessen and Max A. Viergever, editors, *Proc. Medical Image Computing and Computer Assisted Intervention (MICCAI)*, volume 2208 of *Lecture Notes in Computer Science*, pages 734–742, 2001. [cited at p. 49]

[106] D. Louis Collins, Georges Le Goualher, and Alan C. Evans. Non-linear cerebral registration with sulcal constraints. In *Proc. Medical Image Computing and Computer Assisted Intervention (MICCAI)*, pages 974–984, London, UK, 1998. Springer-Verlag. [cited at p. 49]

[107] Kunlin Cao, Kai Ding, Gary E. Christensen, Madhavan L. Raghavan, Ryan E. Amelon, and Joseph M. Reinhardt. Unifying Vascular Information in Intensity-Based Nonrigid Lung CT Registration. In B. Fischer, B.M. Dawant, and C. Lorenz, editors, *Biomedical Image Registration: 4th International Workshop*, LNCS, pages 1–12, 2010. [cited at p. 49, 96, 97]

[108] Pechin Lo, Jon Sporring, Haseem Ashraf, Jesper J.H. Pedersen, and Marleen de Bruijne. Vessel-guided airway tree segmentation: A voxel classification approach. *Medical Image Analysis*, 14(4):527 – 538, 2010. [cited at p. 54]

[109] E.M. van Rikxoort, B. de Hoop, M.A. Viergever, M. Prokop, and B. van Ginneken. Automatic lung segmentation from thoracic computed tomography scans using a hybrid approach with error detection. *Medical Physics*, 36(7):2934–2947, 2009. [cited at p. 64, 96]

[110] E.M. van Rikxoort, B. van Ginneken, M. Klik, and M. Prokop. Supervised enhancement filters: application to fissure detection in chest CT scans. *IEEE Transactions on Medical Imaging*, 27(1):1–10, 2008. [cited at p. 65]

[111] Richard H. Byrd, Peihuang Lu, Jorge Nocedal, and Ciyou Zhu. A limited memory algorithm for bound constrained optimization. *SIAM Journal on Scientific Computing*, 16:1190–1208, 1994. [cited at p. 75]

[112] GL Snider, J Kleinerman, WM Thurlbeck, and ZH Bengali. The definition of epmhysema: report of a National Heart, Lung, and Blood Insitute, division of lung diseases workshop. *American Review of Respiratory Disease*, 132:182–185, 1985. [cited at p. 81]

[113] Lauge Sørensen, Pechin Lo, Haseem Ashraf, Jon Sporring, Mads Nielsen, and Marleen de Bruijne. Learning COPD sensitive filters in pulmonary CT. In *Proc. Medical Image Computing and Computer Assisted Intervention (MICCAI)*, pages 699–706, 2009. [cited at p. 82]

[114] Jan J. Koenderink and Andrea J. Van Doorn. The structure of locally orderless images. *International Journal of Computer Vision*, 31(2-3):159–168, 1999. [cited at p. 83]

[115] Bram van Ginneken and Bart M. ter Haar Romeny. Multi-scale texture classification from generalized locally orderless images. *Pattern Recognition*, 36(4):899–911, 2003. [cited at p. 83]

[116] Kunlin Cao, Gary E. Christensen, Kai Ding, and Joseph M. Reinhardt. Intensity-and-Landmark-Driven, Inverse Consistent, B-Spline Registration and Analysis for Lung Imagery. In *Second International Workshop on Pulmonary Image Analysis*, pages 137–148, 2009. [cited at p. 96]